Journal of Field Robotics

WILEY

RESEARCH ARTICLE OPEN ACCESS

A Study Demonstrating That Using Gravitational Offset to Prepare Extraterrestrial Mobility Missions Is Misleading

Wei Hu[1,2] | Pei Li[2] | Arno Rogg[3] | Alexander Schepelmann[4] | Samuel Chandler[5] | Ken Kamrin[6] | Dan Negrut[2]

[1]School of Ocean and Civil Engineering, Shanghai Jiao Tong University, Shanghai, China | [2]Department of Mechanical Engineering, University of Wisconsin-Madison, Madison, Wisconsin, USA | [3]Ames Research Center, NASA, Mountain View, California, USA | [4]Glenn Research Center – LMT/Mechanisms and Tribology Branch, NASA, Cleveland, Ohio, USA | [5]ProtoInnovations, LLC, Pittsburgh, Pennsylvania, USA | [6]Department of Mechanical Engineering, Massachusetts Institute of Technology, Cambridge, Massachusetts, USA

Correspondence: Dan Negrut (negrut@wisc.edu)

Received: 18 November 2024 | **Revised:** 19 February 2025 | **Accepted:** 2 May 2025

Funding: Support for part of this study was provided by NASA STTR #80NSSC20C0252, National Science Foundation grant OAC2209791 and US Army Research Office, under grants W911NF1910431 and W911NF1810476. The first author was also supported by National Natural Science Foundation of China under grant 12302050.

Keywords: continuous representation model | granular scaling law | rover mobility | rover simulation | smoothed particle hydrodynamics | terramechanics | VIPER

ABSTRACT

Recently, there has been a surge of international interest in extraterrestrial exploration targeting the Moon, Mars, the moons of Mars, and various asteroids. This contribution discusses how current state-of-the-art Earth-based testing for designing rovers and landers for these missions currently leads to overly optimistic conclusions about the behavior of these devices upon deployment on the targeted celestial bodies. The key misconception is that gravitational offset is necessary during the *terramechanics* testing of rover and lander prototypes on Earth. The body of evidence supporting our argument is tied to a small number of studies conducted during parabolic flights and insights derived from newly revised scaling laws. We argue that what has prevented the community from fully diagnosing the problem at hand is the absence of effective physics-based models capable of simulating terramechanics under low-gravity conditions. We developed such a physics-based simulator and utilized it to gauge the mobility of early prototypes of the Volatiles Investigating Polar Exploration Rover. This contribution discusses the results generated by this simulator, how they correlate with physical test results from the NASA-Glenn SLOPE lab, and the fallacy of the gravitational offset in rover and lander testing. The simulator, which is open-source and publicly available, also supports studies for in situ resource utilization activities, for example, digging, bulldozing, and berming, in low-gravity environments.

1 | Introduction

1.1 | Backdrop

Extraterrestrial exploration has experienced a significant uptick over the last three decades, with NASA alone rolling out several missions, for example, Sojourner (Estier et al. 2000), Spirit and Opportunity (R. V. Morris et al. 2004; Kerr 2009), Curiosity (Voosen 2018), and more recently, Perseverance (Farley et al. 2020). Over the last decade, China has landed rovers on Mars, see Zhurong (Ding et al. 2022a), and on the Moon, see Yutu (Ding et al. 2022b). After the United States, Russia (which landed Moon rovers in the early 1970s), and China—India was the fourth nation to land a rover on the Moon, Pragyan, which was the first to land in the proximity of the south pole, where it carried out a 2-week exploration program in mid-2023. Japan landed the Smart Lander for Investigating Moon rover with mixed success in early 2024, with two reduced-scale rovers, Lunar Exploration Vehicle 1 and Lunar Exploration Vehicle 2, tagging along (Wall 2024).

Due to the abundant presence of granular material on the Moon, Mars, and other moons or asteroids in our solar system, each mission is preceded by *physical testing* on Earth using granular soil conditions—natural sands or simulants, for example, the Mars Global Simulant (MGS-1), Lunar Mare Simulant (LMS-1), Johnson Space Center 1A (JSC-1A), Minnesota Lunar Simulant-1 (MLS-1), and Japanese lunar soil simulant (FJS-1). Simulants attempt to capture the soil conditions that are specific to an area on the celestial body of interest (e.g., He 2010; Taylor et al. 2016; Oravec et al. 2021). A challenging aspect of any testing campaign on Earth has been handling the different gravitational conditions experienced during missions on other celestial bodies. Due to the lower gravitational acceleration on the Moon (approximately 16% of Earth's) and Mars (approximately 38% of Earth's), three corrections have historically been applied to account for these differences: gravity-offload systems (e.g., Han et al. 2010; Dungan et al. 2015; Skonieczny et al. 2016; Valle 2017; Binder et al. 2022; Pearson 2024), reducing the mass of the rover (Carsten et al. 2009; Heverly et al. 2013), and use of lunar simulants designed for mobility studies, for example, Glenn Research Center lunar soil simulant 1 (GRC-1) (Oravec et al. 2010). Note that these techniques can be combined, for example, using a lighter vehicle on GRC-1.

Using gravity offloading and simulants has been and continues to be done for the US and Chinese rovers, and likely for the Indian and Japanese missions. However, recent findings indicate that gravity has a greater impact on performance than just through the vehicle–ground pressure and conducting reduced weight vehicle testing on Earth may lead to overoptimistic results. This has been recently suggested by parabolic flight data reported in Kovács et al. (2020). Consider, for instance, the Curiosity test mentioned in Senatore et al. (2014). The rover was stripped down of accessories, reducing its mass to 340 kg from the nominal 907 kg. Consequently, the weight of the vehicle carried by the soil was identical to the rover's weight on Mars. Then, owing to the higher gravitational pull acting on each soil particle in California's Mojave Desert, the terrain is bound to display a higher yield strength relative to Mars and it could therefore support higher shear stress without yielding, effectively providing an optimistic trafficability assessment. Thus, reducing the mass of the rover, in isolation, is insufficient, unless the soil is changed to account for the lower gravitational pull at work on the targeted planet, moon, or asteroid. Selecting a soil was the focus of the work reported in Oravec et al. (2010)—the GRC-1 regolith simulant was proposed to replicate on Earth the terramechanics experience encountered on the Moon. GRC-1 and GRC-3, designed at Glenn Research Center, were intended to capture terramechanics in the maria regions, with the latter displaying more silt that would compact to higher densities for excavation testing. By adjusting the density and friction angle of the simulant, one could get a spectrum of penetrations in a cone index test that resembled the ones noted by the Apollo astronauts on the Moon. This was a key observation, since the assumption was that trafficability is comparable under different gravitational pulls as long as the terrains' cone index gradients are similar when comparing soils with similar other properties, such as particle size distribution. However, the theory that comparable cone index gradients lead to similar terramechanics under different gravitational pulls has been called into question in Daca (2022) and Daca et al. (2022) and will be revisited here.

Experimental testing in low-gravity environments is poised to benefit in the near future from a technique that has re-emerged after remaining dormant for more than four decades: granular scaling laws (GSLs). Scaling laws enable one to understand how physical properties change with scale. A prime example from fluid dynamics is the use of the Reynolds number in wind tunnel experiments. In Freitag et al. (1970a, 1970b) and Wismer et al. (1976), the authors invoked scaling laws to predict the performance of full-scale off-road vehicles by focusing their attention on scale vehicles. Recently, the topic of GSLs has been revisited, formalized (Slonaker et al. 2017; Zhang et al. 2020) and experimentally validated in Earth-like conditions (Thoesen et al. 2020a, 2020b) as well as in reduced gravity parabolic flights (Daca 2022). Although the newly formulated GSLs have not yet been used in extraterrestrial missions, they can provide a breakthrough by bridging disparate gravitational response scenarios. Herein, we employ GSLs to corroborate computer-simulated terramechanics predictions with experimental data.

This contribution is concerned with how rovers and landers are tested on Earth before deployment, emphasizing the value of utilizing physics-based simulation. Shifting the focus from terramechanics physical testing to computer simulation, the "production" approaches used to predict extraterrestrial mobility are almost exclusively rooted in the seminal work of Bekker, Wong, and Reece. The Bekker–Wong formula, $p = \left(\frac{K_c}{b} + K_\phi\right) z^n$, relates the normal pressure p to the sinkage z for a wheel of width b using a semiempirical, experiment-based curve fitting with parameters K_c, K_ϕ, and n (Bekker 1956). The Janosi–Hanamoto formula, $\tau = \tau_{\max}(1 - e^{-J_s/K_s})$, or variants thereof, subsequently use the pressure p to evaluate the shear stress τ between the wheel and terrain (Janosi and Hanamoto 1961). Specifically, τ depends on $\tau_{\max} = c + p \tan \varphi$, the accumulated shear displacement J_s, the cohesion coefficient c, internal friction angle φ, and the so-called Janosi parameter or slip modulus K_s. This phenomenological approach has its origins in work done in conjunction with military vehicles (Bekker 1956; Hegedus 1960; Janosi and Hanamoto 1961; Wong and Reece 1967a, 1967b; Bekker 1969). In planetary exploration, a broad family of terramechanics models have built off the Bekker–Wong model (Iagnemma et al. 2004; Shibly et al. 2005; Bauer et al. 2005; Ishigami et al. 2007; Krenn et al. 2008; Krenn and Hirzinger 2009; Krenn and Gibbesch 2011; Tang et al. 2020; Serban et al. 2022).

For most simulations, a Bekker–Wong/Janosi–Hanamoto (BWJH) type model runs at a real-time factor (RTF) of 1 and below, which indicates faster than real-time operation (the RTF is defined as the amount of time a computer has to work to simulate 1 s of system evolution). Thus, the BWJH models are suitable for expeditious simulations aimed at testing autonomy algorithms, for example, state estimators, path planners, and control policies (Chiang et al. 2010; DeDonato et al. 2015). The BWJH results are satisfactory under three main assumptions: the wheel sinkage is small, slip ratio is low, and the wheel geometry is close to a cylinder without lugs or grousers (Smith et al. 2014; Meirion-Griffith and Spenko 2011). However, there are several problems with employing the BWJH class of models for *predictive* extraterrestrial terramechanics studies; that is, simulating scenarios that would predict mobility on the Moon, for instance. To start with, low-gravity terramechanics is poorly understood and subject to ongoing research (Kobayashi et al. 2010; Daca 2022). The BWJH model abstraction, a phenomenological/semiempirical framework, has been established in conjunction with mobility in Earth gravitation and the community discarded the role of gravity (Ding et al. 2015). When it became apparent that the BWJH class should factor in gravity aspects, corrections have been attempted (Wong 2012), yet the ensuing methodology called for yet additional empirical parameters that were hard to produce. Thus, amending the BWJH class of models needed additional calibration, which went beyond the bevameter test employed to produce the stock BWJH parameters. It is also noted that the bevameter test is involved, not standardized, and calls for a heavy and bulky apparatus. Moreover, results associated with bevameter tests carried out on Earth (e.g., Apfelbeck et al. 2011; Edwards et al. 2017) have not been correlated to low-gravity BWJH model parameters. Finally, the BWJH calibration problem is indeterminate (multiple combinations of parameters lead to similar results) and is prone to overfitting, leading to solutions that are highly specific to one regime (Agarwal et al. 2019).

In lieu of bevameter tests, there have been a posteriori BWJH parameter identification efforts done while the rover operated in situ, see, for instance, the recent ChangE-4 mission that deployed the Yutu-2 rover to the Moon (Ding et al. 2022b, 2024). Similar BWJH identification efforts, Earth-bound though, are reported in Iagnemma et al. (2002) and Ojeda et al. (2006). The nature of being a posteriori, that is, the rover operates at the time when model parameters are calibrated, curtails the effectiveness of the BWJH insofar as the mission preparation and rover *design* are concerned. The BWJH can be employed, upon meeting the three aforementioned assumptions, to ground-control an ongoing mission. However, changing the rover wheel or celestial body of destination would require a new BWJH model that would need to be calibrated from scratch yet again.

Being semiempirical, the BWJH model requires additional adjustments to account for attributes, such as nontrivial grousers (Irani et al. 2011), steering (Ishigami et al. 2007), light weight and/or small size (Meirion-Griffith and Spenko 2011), and so forth. The BWJH models are documented as lacking in handling of irregular terrain for which the equivalent geometric factor b is hard to gauge since the interaction with irregular terrain is complex and nonstationary. The choice of b is further complicated by the use of flexible wheels, employed, for instance, on the Lunar Roving Vehicles of the Apollo 15–17 missions. Finally, the terrain in BWJH lacks any dynamic response—there is no material and therefore mass movement associated with soil and its deformation; the terrain is simply a force element that prevents the sinking of the wheel and yields a tractive force. As such, dig-in and material ejection cannot be captured. For a list of other limitations and mitigating approaches (see Rodríguez-Martínez et al. 2019).

In a broader context, beyond the class of BWJH models, there are two other terramechanics simulation options: approaches that embrace a continuous representation model (CRM) (Sulsky et al. 1994; Bardenhagen et al. 2000; Bui et al. 2008; W. Chen and Qiu 2012; Chauchat and Médale 2014; Ionescu et al. 2015; Dunatunga and Kamrin 2017); and fully resolved approaches, in which the motion of the particles that constitute soil is tracked forward in time using the so-called discrete element method (DEM) (Cundall and Strack 1979; Iwashita and Oda 1999; Jensen et al. 1999). The DEM approach is slow but accurate; the CRM lies in between BWJH and DEM, both in terms of speed and accuracy.

When a wheel operating on granular soils features complex lugs or grouser geometries, or experiences very high slip ratios, the DEM can be relied upon for accurate numerical results (Johnson et al. 2015; Ucgul et al. 2015; Zhao and Zang 2017; Recuero et al. 2017). However, since many engineering problems can involve billions of discrete grains, the computational cost of a fully resolved DEM simulation can become prohibitively high. The RTF of DEM terramechanics simulations can be in the range of 3000–15,000 (see, e.g., Recuero et al. 2017). By comparison, the RTF for CRM terramechanics simulations can be as low as 30–150 (Hu et al. 2022). Another strength of CRM is that it is a physics-based approach in which the input parameters, for example, density, friction angle, stiffness, shear modulus, cohesion can be easily obtained (see, e.g., He 2010), or estimated. Consequently, little to no parameter calibration is needed before running the simulations. The three attractive attributes of CRM—speed, accuracy, and setup convenience, come at the price of a more involved solution methodology. Indeed, being the solution of a time-dependent set of partial differential equations, the continuum problem is spatially discretized using either a finite element method (FEM) (Chauchat and Médale 2014; Ionescu et al. 2015); or a meshless solution, for example, the material point method (MPM) (Sulsky et al. 1994; Bardenhagen et al. 2000; Soga et al. 2016; Baumgarten and Kamrin 2019; Agarwal et al. 2019), or the smoothed particle hydrodynamics (SPH) method (Bui et al. 2008; W. Chen and Qiu 2012; Nguyen et al. 2017; Hurley and Andrade 2017; Xu et al. 2019; J.-Y. Chen et al. 2020; Hu et al. 2021). Since the soil is subject to plastic flow with large deformation at high slip ratio, ill-shaped FEM elements can lead to numerical instabilities or require costly remeshing operations, which places meshless methods at an advantage.

In this contribution, we report on a new simulation-anchored framework for designing rover and lander missions. The terramechanics modeling methodology adopted is based on the CRM (Hu et al. 2021) due to its accuracy and efficiency traits, and employs the SPH spatial discretization of the equations of motion. Our contribution is fourfold—specifically, we: established CRM as a viable approach for terramechanics simulation; implemented an open-source publicly available CRM simulator validated against Volatiles Investigating Polar Exploration Rover (VIPER)-related experimental data; demonstrated that the physics-based simulator is predictive—it produces results that match experimental test results and obey the scaling predicted by GSL; most importantly, demonstrated that the simulator reveals misconceptions in the way the physical testing of rovers is carried out today.

1.2 | Experimental Setup

The study discussed in this contribution is summarized in Figure 1. We present results for both single-wheel and full-rover tests; the rover used is a 1/6 mass replica of VIPER. The validation experimental test data were collected at NASA's SLOPE lab. The deformable terrain was modeled using the CRM approach; details can be found in Section 1.3. Being a physics-based methodology, the CRM model parameters are identical to the material parameters associated with the GRC-1 (Oravec et al. 2010) and GRC-3 (He et al. 2013) lunar soil simulant used in NASA's SLOPE lab. In other words, compared with the semiempirical BWJH approach, the parameter calibration needs are significantly reduced as the parameters needed are friction angle, bulk density, and so forth; that is, parameters with immediate physical meaning. The single-wheel simulations were run in "VV"-mode, where both the translational "V"elocity and angular "V"elocity of the wheel were controlled to yield a certain wheel slip; and then in "slope"-mode, where the angular velocity of the wheel was constant, and the translational velocity was measured once the wheel reached a steady state on a terrain with a fixed slope. For the full rover, all simulations were in slope-mode. The single-wheel test rig and the rover were modeled as multibody systems, thus capturing the full nonlinear dynamics of the system. All simulations were conducted in a cosimulation framework with the multibody dynamics solved using a multicore central processing unit (CPU) and the CRM terramechanics solved on a graphics processing unit (GPU). The slope/slip and power/slip relationships obtained in the simulation were validated against experimental data.

In the simulations performed for both single wheel and full rover, two modules come into play in the cosimulation framework implemented in the open-source software Chrono (Tasora et al. 2016; Project Chrono Team 2020). One is a multibody dynamics simulation engine, which is used to propagate forward in time the motion of the solid bodies, for example, the dynamics of a single wheel or the full rover. The frictional contact between the rigid bodies is handled therein using a differential variational inequality approach (Pazouki et al. 2017; Negrut et al. 2018). The second module handles the dynamics of the granular lunar terrain, which is accomplished using the CRM approach. Since the SPH particles used to discretize the CRM simulation domain are usually much larger than the actual terrain grains, the degree of freedom count is significantly reduced, which explains the major CRM simulation speed gains over DEM simulation. The dynamics of the SPH particles were integrated forward in time using GPU acceleration. Since the dynamics of the rover and the terrain systems were solved separately in two different simulation engines, one running on the CPU and one on the GPU, a communication was required between these two hardware assets to enforce the coupling effect, that is, the wheel–soil interaction. Figure 2 illustrates the developed cosimulation framework. At

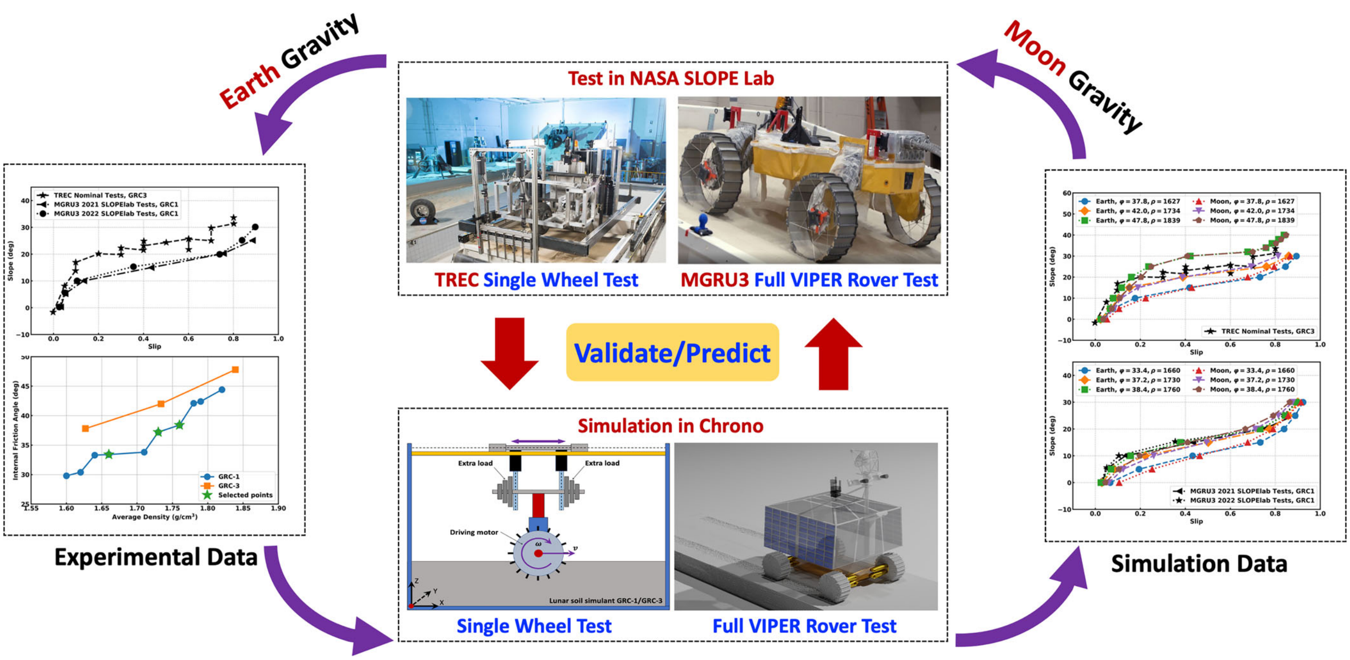

FIGURE 1 | Schematic view of the workflow: experimental test results are used to validate the simulator, which is subsequently used to predict the VIPER rover's performance on the Moon. The experimental data were generated at NASA's SLOPE lab with tests performed under Earth gravity. The same tests were conducted in the physics-based Chrono simulator, to judge its predictive traits before using it to produce results under Moon gravity. GRC, Glenn Research Center; MGRU3, Moon Gravitation Representative Unit 3; TREC, Traction and Excavation Capabilities; VIPER, Volatiles Investigating Polar Exploration Rover. [Color figure can be viewed at wileyonlinelibrary.com]

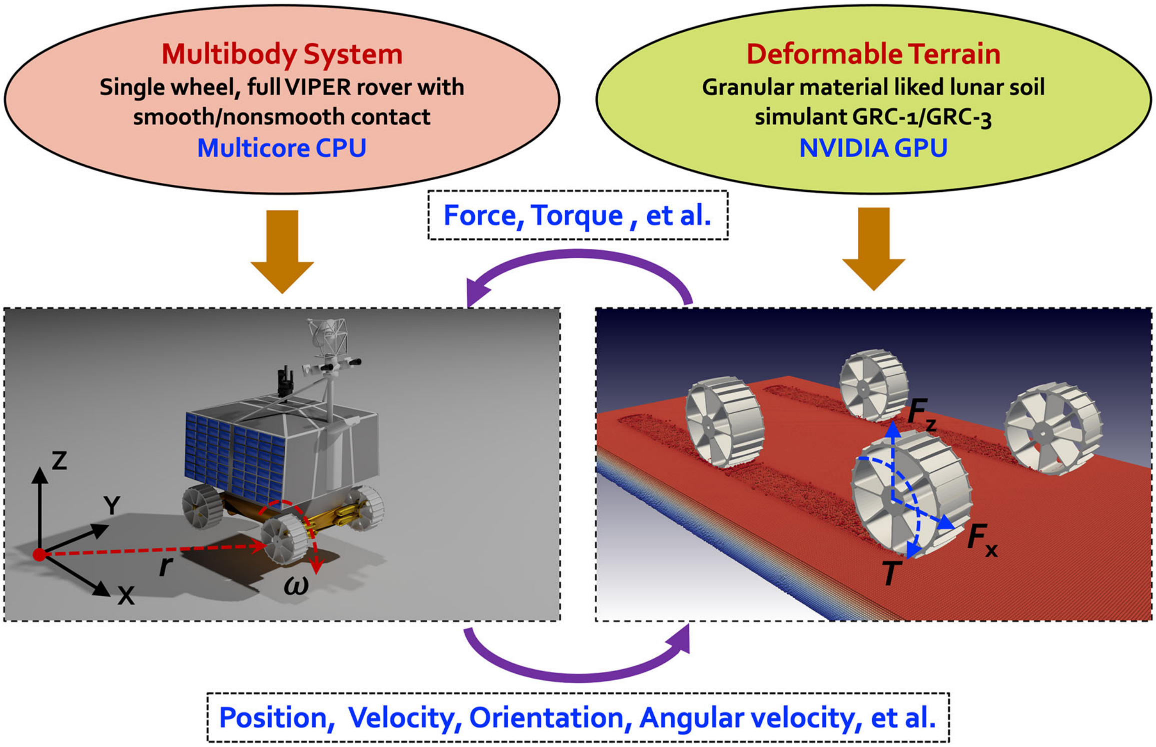

FIGURE 2 | The cosimulation framework employed: the rover was modeled as a multibody system whose dynamics was solved using a multicore CPU. The deformable terrain was modeled as a continuum whose dynamics was solved using GPU computing. The two modules communicated passing force and torque information from the terrain to the rover; and position, velocity, orientation, and angular velocity coming from each wheel and going to the terrain CRM solver. CPU, central processing unit; CRM, continuous representation model; GPU, graphics processing unit; GRC, Glenn Research Center; VIPER, Volatiles Investigating Polar Exploration Rover. [Color figure can be viewed at wileyonlinelibrary.com]

each time step, the dynamics of terrain was solved first, hence the force and torque that was applied from the soil to the wheel can be calculated and passed from the GPU memory to the CPU memory. Then the dynamics of the rover system was solved with the external force applied from the terrain side. Once the new position, velocity, orientation, and angular velocity of each wheel were updated, they were passed back to the GPU memory to advance in time the state of the terrain.

1.3 | Granular Scaling Laws

Two important points highlighted in this contribution are as follows: (a) by careful experimental design, terramechanics in low-gravity environments can be correlated with terramechanics under Earth's gravity and (b) CRM serves as a predictive method for understanding rover terramechanics over a range of gravitational accelerations. These claims are supported by results and observations that align with the expectations spelled out by the GSLs, which are summarized below. Several accounts are available for these laws, herein the discussion is anchored by recent work reported in Zhang et al. (2020). The two laws of interest pertain to the scaling of (i) the power necessary to produce a certain motion of an implement, for example, a wheel; and (ii) the translational velocity experienced by the implement. Specifically, the scaling laws assert the existence of a function $\mathbf{\Psi}$ of five inputs that produces two outputs, the latter being the scaling of the power P and longitudinal velocity V associated with the terramechanics of an implement (here a wheel) (Zhang et al. 2020):

$$\begin{bmatrix} \dfrac{P}{Mg\sqrt{Lg}} \\ \dfrac{V}{\sqrt{Lg}} \end{bmatrix} = \mathbf{\Psi}\left(\sqrt{\frac{g}{L}}t, f, \frac{g}{L\omega^2}, \frac{\rho_0 DL^2}{M}, \theta\right). \tag{1}$$

Above, it is assumed that the granular material is cohesionless (see Zhang et al. 2020 for cohesive terrain scenarios), L is a characteristic length (for a wheel, its effective radius), M is the total mass, D is the width, ω is the angular velocity, f is a shape factor, ρ_0 is the bulk density in dense state, g is the gravitational pull, and θ is the tilt of the slope negotiated by the wheel. The laws in Equation (1) states that if two experiments are carried out, with a set of parameters indexed by subscripts 1 and 2, respectively, and if $\frac{\rho_{01}D_1L_1^2}{M_1g_1} = \frac{\rho_{02}D_2L_2^2}{M_2g_2}$, $\frac{g_1}{L_1\omega_1^2} = \frac{g_2}{L_2\omega_2^2}$, $f_1 = f_2$, $\sqrt{\frac{g_1}{L_1}}t_1 = \sqrt{\frac{g_2}{L_2}}t_2$, and $\theta_1 = \theta_2$, then the corresponding quantities with "1" and "2" on the left side of Equation (1) are identical for the two experiments. Consequently, if P_1 and V_1 are measured in experiment "1", they can be used to estimate the power and velocities in the experiment indexed by the subscript "2". In Section 3.2, the subscript "1" will be implicitly associated with Earth tests, while "2" with Moon tests.

2 | Materials and Methods

To resolve the dynamics of the deformable terrain in its two-way coupling with the rover's wheels movement, we employed a homogenization of the granular-like lunar soil and used an elastoplastic CRM approach (Dunatunga and Kamrin 2017).

The CRM solution is obtained using the SPH method (Lucy 1977; Gingold and Monaghan 1977). The two-way coupling between terrain and implements is discussed in Hu et al. (2021, 2022); the approach therein captures large deformation of the granular material terrain and large overall three-dimensional (3D) motion of the solid bodies. The interaction between implements and terrain is posed and solved as a fluid–solid interaction problem using so-called boundary-conditions enforcing (BCE) particles rigidly attached to the boundary of the solid bodies. To connect the dynamics of the granular material with the update in the stress field, we employ the constitutive law proposed in Dunatunga and Kamrin (2015). Note that in CRM, one can replace the SPH-based spatial discretization of the equations of motion with an alternative one anchored by the MPM, likely yielding equally good results (Dunatunga and Kamrin 2015; Haeri and Skonieczny 2022).

The physical results reported were obtained at NASA's SLOPE lab with tests performed under Earth gravity. In lieu of lunar regolith, the soil simulants used were GRC-3 and GRC-1. First, single-wheel and full-rover physical testing was carried out to obtain the slope/slip and power/slip maps reported herein. Subsequently, digital twins were built and the simulations were carried out in Chrono; for the rover test, a full multibody system was set up to match the Moon Gravitation Representative Unit 3 (MGRU3) rover. For the wheel test rig or full-rover simulations, the soil parameters used were those of the actual GRC-3 and GRC-1 simulant. The simulator uses a cosimulation framework in which the wheel/rover dynamics was solved on a multicore CPU chip while the terrain dynamics was solved at the same time using an NVIDIA GPU. A small amount of data was CPU–GPU exchanged at each numerical integration time step to enforce the coupling between wheel and soil. Changing from Earth conditions to Moon conditions was as simple as changing one line of code, from Earth's gravitational acceleration to that of the Moon. Due to the lack of lunar physical test data, we could not validate the accuracy of the Moon simulation results directly. The Moon gravity simulation results matched well the results obtained using Earth gravity if one analyzes the data through the lens of the scaling law theory.

In relation to the materials and methods used, one caveat is that the results reported were obtained using the regolith simulants GRC-1 and GRC-3. As pointed out, there is an ongoing debate in the community about the suitability of using these simulants. Providing a comprehensive answer to this question falls outside the scope of this contribution. However, there are two relevant and salient points relevant in this context. First, the actual results reported, for example, the slope/slip curves, might not be identical to the results that will be noted on the Moon. This is because the terrains (the one used in simulation and the real one on the Moon) are likely different. The second salient point is that one can nonetheless rely on a *physics-based* simulator to conduct a battery of simulations sweeping over ranges of likely terrain properties (bulk densities, friction angles, etc.) to obtain a comprehensive image of the possible performance of the rover. In time, once the geomechanics attributes of the lunar soil become available, the physics-based simulator will produce results of lesser uncertainty.

2.1 | Overview of the CRM Methods

For the CRM approach used in this study, we employ a homogenization of the granular material and use a hypoelastoplastic continuum model to capture the dynamics of the deformable lunar soil terrain (Dunatunga and Kamrin 2015). Herein, the CRM solution is obtained using the SPH method, which is a Lagrangian particle-based solution that requires no background grid (Lucy 1977; Gingold and Monaghan 1977). The state information is advected with the SPH particles, and the dynamic equations are enforced at the location of the SPH particles. The particles move based on the interactions among neighbor particles and the external forces, for example, gravity. The SPH method has proven effective and efficient in simulating granular material problems with large deformation (Nguyen et al. 2017; Hurley and Andrade 2017; Hu et al. 2021, 2022). The background assumption of the approach used to model the terrain is that the deformable soil can be homogenized as a continuum, from where the CRM name of the method. The homogenization works well for dry sand on Earth, granular soil on the Moon, or in general, for any granular material for which the grain size is relatively uniform and the number of particles is substantial. Objects whose size is large relative to that of the granular material particle are treated outside the CRM approach through BCE markers, for two-way coupling. This is the case of a rover's wheels, an excavator's bucket, a blade, or a rock that is placed on the deformable terrain. For the latter, if a rover wheel moves over the rock, there is a coupling between the dynamics of the vehicle, rock, and granular terrain, the latter handled in this study via CRM terramechanics. Capturing in a physics-based framework the interplay between the CRM terrain and other implements/artifacts falls outside of the scope of this contribution, and the interested reader is referred to (Hu et al. 2021, 2022)

In CRM, the problem unknowns, that is, the field velocity vector $\mathbf{u}$, and the Cauchy stress tensor $\boldsymbol{\sigma}$, enter the mass and momentum balance equations as

$$\begin{cases} \frac{d\mathbf{u}}{dt} = \frac{\nabla \cdot \boldsymbol{\sigma}}{\rho} + \mathbf{f}_b, \\ \frac{d\rho}{dt} = -\rho \nabla \cdot \mathbf{u}, \end{cases} \tag{2}$$

where ρ is the density of the deformable terrain, and $\mathbf{f}_b$ represents external forces, for example, the gravity force. The total stress tensor $\boldsymbol{\sigma} \in \mathbb{R}^{3\times3}$ is split in two components expressed as $\boldsymbol{\sigma} \equiv -p\mathbf{I} + \boldsymbol{\tau}$, where $\boldsymbol{\tau}$ is the deviatoric component of the total stress tensor and p is the pressure which can be calculated from the trace of the total stress tensor as $p = -\frac{1}{3}\mathrm{tr}(\boldsymbol{\sigma}) = -\frac{1}{3}(\sigma_{xx} + \sigma_{yy} + \sigma_{zz})$. For closure, a stress rate tensor formula is employed. We use Hooke's law, as well as the work described in Dunatunga and Kamrin (2015), Monaghan (2000), Gray et al. (2001), and Yue et al. (2015) to express the objective total stress rate tensor as

$$\frac{d\boldsymbol{\sigma}}{dt} = \dot{\boldsymbol{\phi}} \cdot \boldsymbol{\sigma} - \boldsymbol{\sigma} \cdot \dot{\boldsymbol{\phi}} + 2G\left[\dot{\boldsymbol{\varepsilon}} - \frac{1}{3}\mathrm{tr}(\dot{\boldsymbol{\varepsilon}})\mathbf{I}\right] + \frac{1}{3}K\mathrm{tr}(\dot{\boldsymbol{\varepsilon}})\mathbf{I}. \tag{3}$$

In Equation (3), when the material is not subject to plastic flow, the elastic strain rate tensor $\dot{\boldsymbol{\varepsilon}}$ of the granular material is defined as $\dot{\boldsymbol{\varepsilon}} = \frac{1}{2}[\nabla \mathbf{u} + (\nabla \mathbf{u})^{\intercal}]$; the rotation rate tensor is expressed as $\dot{\boldsymbol{\phi}} = \frac{1}{2}[\nabla \mathbf{u} - (\nabla \mathbf{u})^{\intercal}]$. Herein, G and K denote the shear modulus and bulk modulus of the granular material-like deformable terrain, respectively, and $\mathbf{I}$ is the identity matrix. It is noted that the expression of the elastic strain rate tensor given above only works in cases without a plastic flow. Once the granular material starts to flow, the elastic strain rate tensor is defined as

$$\dot{\boldsymbol{\varepsilon}} = \frac{1}{2}[\nabla \mathbf{u} + (\nabla \mathbf{u})^{\intercal}] - \frac{\dot{\lambda}}{\sqrt{2}} \frac{\boldsymbol{\tau}}{\bar{\tau}}, \tag{4}$$

in which the second term on the right-hand side comes from the contribution of the plastic flow of the continuum representation of the granular material. Therein, $\dot{\lambda}$ and $\bar{\tau}$ are the plastic strain rate and equivalent shear stress, respectively (Dunatunga and Kamrin 2015). Briefly summarized, the model used is an incompressible, hypoelastic–plastic continuum model, with nonassociated plasticity.

We use the SPH method to spatially discretize the mass and momentum balance equations in Equation (2) and the expression of the total stress rate tensor in Equation (3). In SPH, the simulation domain (including the deformable granular material terrain, solid bodies, and wall boundaries) is discretized using SPH and BCE particles. The former are used in conjunction with the deformable granular material terrain, with which they advect. The motion of the SPH particles is obtained by solving the governing equations, see Equations (2) and (3). Conversely, the motion of the BCE particles is tied to that of the solid bodies, to which they are rigidly attached. Their role is to couple the motion of the SPH particles to the motion of the solid bodies (Hu et al. 2021).

According to the SPH method, the value of a function f at the position of particle i can be approximated as (Monaghan 2005):

$$f_i = \sum_j f_j W_{ij} \mathcal{V}_j, \tag{5}$$

where W_{ij} is a kernel function, and $\mathcal{V}_i$ is the volume of particle i, defined as $\mathcal{V}_i = (\sum_j W_{ij})^{-1}$. Thus, the mass associated with particle i can be obtained as $m_i = \rho_i \mathcal{V}_i$. Herein, we use a cubic spline kernel function:

$$W_{ij} = W(\mathbf{r}_{ij}) = \alpha_{\mathrm{d}} \cdot \begin{cases} \frac{2}{3} - R^2 + \frac{1}{2}R^3, & 0 \le R < 1, \\ \frac{1}{6}(2-R)^3, & 1 \le R < 2, \\ 0, & R \ge 2 \end{cases} \tag{6}$$

for which the relative position between particles i and j is defined as $\mathbf{r}_{ij} = \mathbf{x}_i - \mathbf{x}_j$, with $\mathbf{x}_i$ and $\mathbf{x}_j$ being the positions of particle i and j, respectively. For a 3D problem, $\alpha_{\mathrm{d}} = 3/(2\pi h^3)$. The scaled length parameter R is defined as $R = r_{ij}/h$, where r_{ij} is the length of the vector $\mathbf{r}_{ij}$, and h the characteristic smoothing length (one to two times the initial particle spacing Δx). In light of Equation (6), a field variable (e.g., velocity $\mathbf{u}$ or density ρ) at the position of particle i receives contributions from the values at all neighbor particles j according to Equation (5) as long as $j \in \mathcal{N}_{h,i} \equiv \{\mathbf{x}_j : r_{ij} < 2h\}$.

For the gradient ∇f evaluated at the position of SPH particle i, both consistent and inconsistent discretizations are available (Fatehi and Manzari 2011). While computationally slightly more expensive, the consistent SPH discretisation

$$\nabla f_i = \sum_j (f_j - f_i)(\mathbf{G}_i \cdot \nabla_i W_{ij}) \mathcal{V}_j \tag{7}$$

gives higher accuracy and is used herein. The gradient of the kernel function W_{ij} with respect to the position of particle i is expressed as

$$\nabla_i W_{ij} = \frac{\alpha_{\mathrm{d}}}{h} \frac{\mathbf{r}_{ij}}{r_{ij}} \begin{cases} -2R + \frac{3}{2}R^2, & 0 \le R < 1, \\ -\frac{1}{2}(2-R)^2, & 1 \le R < 2, \\ 0, & R \ge 2 \end{cases}$$

In Equation (7), $\mathbf{G}_i \equiv -[\sum_j \mathbf{r}_{ij} \otimes \nabla_i W_{ij} \mathcal{V}_j]^{-1} \in \mathbb{R}^{3\times 3}$ is a symmetric correction matrix associated with particle i. With $\mathbf{G}_i$ being involved in the discretization of the gradient operator, an exact gradient for a linear function f can be guaranteed regardless of the ratio of $h/\Delta x$ (Fatehi and Manzari 2011), where Δx is the initial SPH discretization spacing. This higher accuracy allows one to use a relatively smaller h, thus saving computational cost (see, e.g., Hu et al. 2019).

Hence, the consistent discretizations of the momentum balance and continuity equations are obtained by substituting Equation (2) into Equation (7), which yields

$$\frac{d\mathbf{u}_i}{dt} = \frac{1}{\rho_i} \sum_j (\boldsymbol{\sigma}_j - \boldsymbol{\sigma}_i) \cdot \mathbf{b}_{ij} + \mathbf{f}_{b,i}, \tag{8}$$

$$\frac{d\rho_i}{dt} = -\rho_i \sum_j (\mathbf{u}_j - \mathbf{u}_i) \cdot \mathbf{b}_{ij}. \tag{9}$$

Similarly, the consistent discretization of the rotation rate and strain rate tensors assumes the expression

$$\dot{\boldsymbol{\phi}}_i = \frac{1}{2} \sum_j \left[\mathbf{u}_{ji} \mathbf{b}_{ij}^{\intercal} - \left(\mathbf{u}_{ji} \mathbf{b}_{ij}^{\intercal} \right)^{\intercal} \right], \tag{10}$$

$$\dot{\boldsymbol{\varepsilon}}_i = \frac{1}{2} \sum_j \left[\mathbf{u}_{ji} \mathbf{b}_{ij}^{\intercal} + \left(\mathbf{u}_{ji} \mathbf{b}_{ij}^{\intercal} \right)^{\intercal} \right], \tag{11}$$

where $\mathbf{b}_{ij} \equiv \mathbf{G}_i \cdot \nabla_i W_{ij} \mathcal{V}_j$. Finally, the consistent discretization of the total stress rate tensor is obtained by substituting Equations (10) and (11) into Equation (3), which yields

$$\begin{aligned} \frac{d\boldsymbol{\sigma}_i}{dt} = \frac{1}{2} & \left\{ \sum_j \left[\mathbf{u}_{ji} \mathbf{b}_{ij}^{\intercal} - \left(\mathbf{u}_{ji} \mathbf{b}_{ij}^{\intercal} \right)^{\intercal} \right] \boldsymbol{\sigma}_i - \boldsymbol{\sigma}_i \sum_j \left[\mathbf{u}_{ji} \mathbf{b}_{ij}^{\intercal} - \left(\mathbf{u}_{ji} \mathbf{b}_{ij}^{\intercal} \right)^{\intercal} \right] \right\} \\ & + G \left\{ \sum_j \left[\mathbf{u}_{ji} \mathbf{b}_{ij}^{\intercal} + \left(\mathbf{u}_{ji} \mathbf{b}_{ij}^{\intercal} \right)^{\intercal} \right] \right. \\ & \left. - \frac{1}{3} \mathrm{tr} \left(\sum_j \left[\mathbf{u}_{ji} \mathbf{b}_{ij}^{\intercal} + \left(\mathbf{u}_{ji} \mathbf{b}_{ij}^{\intercal} \right)^{\intercal} \right] \right) \mathbf{I} \right\} \\ & + \frac{1}{6} K \left\{ \mathrm{tr} \left(\sum_j \left[\mathbf{u}_{ji} \mathbf{b}_{ij}^{\intercal} + \left(\mathbf{u}_{ji} \mathbf{b}_{ij}^{\intercal} \right)^{\intercal} \right] \right) \mathbf{I} \right\}. \end{aligned} \tag{12}$$

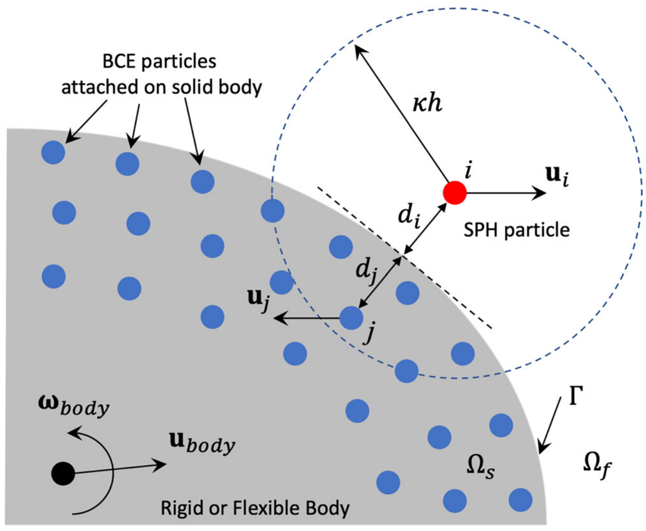

FIGURE 3 | SPH particles and BCE particles close to the solid body or wall boundary. The Dirichlet boundary condition is imposed by extrapolating the velocities to the BCE particles. BCE, boundary-conditions enforcing; SPH, smoothed particle hydrodynamics. [Color figure can be viewed at wileyonlinelibrary.com]

2.2 | Wheel–Soil Interaction

In this study, a two-way coupling approach is modeled by imposing a Dirichlet (no-slip and no-penetration) boundary condition (BC) for the deformable granular material terrain at the solid boundary (moving wheels or fixed wall). To accurately impose a Dirichlet BC for the granular material's velocity, a full support domain contained in $(\Omega_f \cup \Omega_s)$ should be attained to guarantee accurate SPH approximation for particles close to the boundary Γ. To this end, as shown in Figure 3, we follow the strategy proposed in Takeda et al. (1994), J. P. Morris et al. (1997), Holmes et al. (2011), Pan et al. (2017), and Hu et al. (2017) to generate several layers of BCE particles in the solid area Ω_s close to the boundary Γ. The velocities of the BCE particles can be linearly extrapolated from the SPH particles' velocities close to the boundary, that is,

$$\mathbf{u}_j = \frac{d_j}{d_i}(\mathbf{u}_B - \mathbf{u}_i) + \mathbf{u}_B, \tag{13}$$

where d_i and d_j represent the perpendicular distances to the solid boundary Γ for an SPH particle i and a BCE particle j, respectively. Here, $\mathbf{u}_B$ denotes the velocity at the solid boundary, which is expressed as

$$\mathbf{u}_B = \mathbf{u}_{body} + \boldsymbol{\omega}_{body} \times \mathbf{r}_c(\mathbf{x}), \tag{14}$$

where $\mathbf{u}_{body}$ and $\boldsymbol{\omega}_{body}$ are the translational and angular velocities of the solid body (e.g., the moving rover wheel), respectively; and $\mathbf{r}_c(\mathbf{x})$ denotes the vector from the center of mass (e.g., the wheel center) of the solid body to the location $\mathbf{x}$ at the boundary Γ. Note that the velocities of the BCE particles extrapolated from that of the SPH particles and the solid boundary are only used to enforce the Dirichlet BC; these velocities cannot be used to advect the BCE particles since they will move along with the solid body to which they are rigidly attached.

For the total stress tensor $\boldsymbol{\sigma}_j$ at the position of a BCE particle j, we follow the approach in Zhan et al. (2019) to extrapolate it from the SPH particles' total stress tensor close to the boundary Γ, that is,

$$\boldsymbol{\sigma}_j = \frac{\sum_{i\in\Omega_f}\boldsymbol{\sigma}_i W_{ji} + [diag(\mathbf{f}_b - \mathbf{f}_j)]\sum_{i\in\Omega_f}\rho_i[diag(\mathbf{r}_{ji})]W_{ji}}{\sum_{i\in\Omega_f}W_{ji}}, \tag{15}$$

where $\mathbf{r}_{ji} = \mathbf{x}_j - \mathbf{x}_i$, the function $diag(\mathbf{f}_b - \mathbf{f}_j)$ creates a diagonal matrix from the vector $\mathbf{f}_b - \mathbf{f}_j$ and so does the function $diag(\mathbf{r}_{ji})$, $\mathbf{f}_b$ is the body force of the granular material (e.g., the gravity), and $\mathbf{f}_j$ is the inertial force associated with the BCE particle j and can be evaluated as

$$\mathbf{f}_j = \dot{\mathbf{u}}_{body} + \dot{\boldsymbol{\omega}}_{body} \times \mathbf{r}_{jc} + \boldsymbol{\omega}_{body} \times (\boldsymbol{\omega}_{body} \times \mathbf{r}_{jc}), \tag{16}$$

where $\mathbf{r}_{jc}$ is the vector from the solid body's center of mass to the position of the BCE particle j. The total force $\mathbf{F}_{body}$ and torque $\mathbf{T}_{body}$ exerted by the deformable terrain upon the solid body is then calculated by summing the forces contributed by the SPH particles onto the BCE particles as described in the conservative SPH method (Bian and Ellero 2014), that is,

$$\mathbf{F}_{body} = \sum_{j\in\Omega_s} m_j\dot{\mathbf{u}}_j \quad \text{and} \quad \mathbf{T}_{body} = \sum_{j\in\Omega_s} \mathbf{r}_{jc} \times (m_j\dot{\mathbf{u}}_j). \tag{17}$$

2.3 | Update of Field Variables

In this study, the field variables (e.g., the velocity, position, and total stress tensor) of the SPH particles are updated using an explicit predictor–corrector time integration scheme with second-order accuracy (Monaghan 1989, 1994). There are two half steps involved in this integration scheme for each time step. In the first half step, an intermediate value of velocity $\bar{\mathbf{u}}_i$, position $\bar{\mathbf{x}}_i$, and total stress tensor $\bar{\boldsymbol{\sigma}}_i$ are first predicted at $t + \frac{\Delta t}{2}$. Using predicted values, Equations (8), (12), and (18) are evaluated again to update the velocity, position, and total stress tensor to the corrected values. Finally, the field variables of the SPH particles are updated based on the initial and corrected values at $t + \Delta t$. More details about the interaction scheme for granular material dynamics can be found in Hu et al. (2021).

To enforce the condition that the particles advect at a velocity close to an average velocity of their neighboring particles, the so-called Extended Smoothed Particle Hydrodynamics (XSPH) technique (Monaghan 1989) is used in this study. According to the XSPH method, the relationship between the displacement of the SPH particle i and its velocity is expressed as

$$\frac{d\mathbf{x}_i}{dt} = \mathbf{u}_i - \xi\sum_j \mathbf{u}_{ij}W_{ij}\mathcal{V}_j, \tag{18}$$

where the second term is a correction term with the coefficient ξ in this study being set to 0.5. More details about the

XSPH method used in granular material dynamics can be found in Hu et al. (2021). Therein, a comprehensive study about how to choose the value of the coefficient ξ was performed by gauging the influence of ξ onto the kinetic energy of the dynamic system.

To accurately update the value of the total stress tensor $\boldsymbol{\sigma}$ of the deformable granular material terrain, we employ an approach originally proposed in MPM (Dunatunga and Kamrin 2015) and apply it within the framework of SPH. The total stress tensor of each SPH particle is first updated explicitly from t to $t + \Delta t$ according to the predictor–corrector scheme described in Monaghan (1989, 1994) and Hu et al. (2021). Once the update is done, at the end of this time step, the total stress tensor is then further corrected based on a four-step post-processing strategy expressed as (i) Calculate the value of p^* and $\boldsymbol{\tau}^*$ according to the value of total stress tensor $\boldsymbol{\sigma}^*$ that is already obtained through the predictor–corrector scheme using Equation (3); (ii) If $p^* < 0$, then simply set $\boldsymbol{\sigma} = \mathbf{0}$ at $t + \Delta t$ and start a new integration time step; (iii) If $p^* > 0$, set $p = p^*$, compute the double inner product of $\boldsymbol{\tau}^*$ as $\bar{\tau}^* = \sqrt{\frac{1}{2}(\tau^*_{\alpha\beta}) : (\tau^*_{\alpha\beta})}$, and compute S_0 as $S_0 = \mu_s p^*$, here, α and β are indices for the stress components; (iv) If $\bar{\tau}^* < S_0$, simply set $\boldsymbol{\tau} = \boldsymbol{\tau}^*$ as the deviatoric component of $\boldsymbol{\sigma}$ at $t + \Delta t$ since no plastic flow occurs at this moment; else, use the Drucker–Prager yield criterion to scale the deviatoric component of $\boldsymbol{\sigma}$ back to the yield surface as $\boldsymbol{\tau} = \frac{\mu p^*}{\bar{\tau}^*}\boldsymbol{\tau}^*$. Here, the friction coefficient used in step (iii) is defined as $\mu = \mu_s + \frac{\mu_2 - \mu_s}{I_0/I + 1}$ (Dunatunga and Kamrin 2015), where μ_s is the static friction coefficient, and μ_2 is the limiting value of μ when $I \to \infty$; I_0 is a material constant that is set to 0.03 in this study; I is the inertial number. For a very low value of I, the friction coefficient μ approaches the minimum value, that is, the static friction coefficient μ_s. Please refer to Jop et al. (2005) for an in-depth discussion of the derivation of this expression and the meaning of the bespoke parameters. More details about the four-step strategy and the parameters' calculation can be found in Hu et al. (2021).

3 | Results

The results reported are organized in two subsections. The first concentrates on single-wheel tests and speaks to the predictive attributes of the simulator, a topic also addressed in Hu et al. (2021, 2024). Section 3.2, which is the linchpin of this contribution, compares single-wheel and rover physical testing results obtained in the SLOPE lab with simulation data produced in Earth and Moon gravitational acceleration conditions. The physical testing and the simulations were conducted using both GRC-1 and GRC-3. Qualitatively, there is no remarkable difference between the GRC-1 and GRC-3 results, be it for single wheel or full rover. Finally, for both GRC-1 and GRC-3, it is noted that the terrain can exhibit a spectrum of friction angles and bulk densities, see Figure 4a for a range of values for the friction angle and bulk density. The experimental results for both single wheel and full rover obtained in NASA SLOPE lab are shown in Figure 4b.

3.1 | VV-Mode: Single-Wheel Experiments

Several single-wheel VV-mode physical and numerical tests were conducted on flat terrain to two ends: produce a plot that relates the DrawBar-Pull (DBP) force to the wheel slip and generate traction slope versus wheel slip plots (see Wong 2009) for a discussion of DBP and these plots. The traction slope associated with a specific wheel slip is calculated as $\arctan(\text{DBP}/N)$, where N is the normal load impressed by the rover wheel on the deformable terrain under Earth gravity. The goal of this exercise was to show that the physics-based simulator is predictive and captures well how key model parameters that have a clear physical meaning, for example, bulk density and friction angle, reflect in the simulated response of the wheel performance. In all tests, physical and numerical, the material was assumed cohesionless.

The physical test was performed at NASA Glenn's SLOPE lab using the Traction and Excavation Capabilities (TREC) Rig, see Figure 1. The experimental results are shown in Figure 4b with

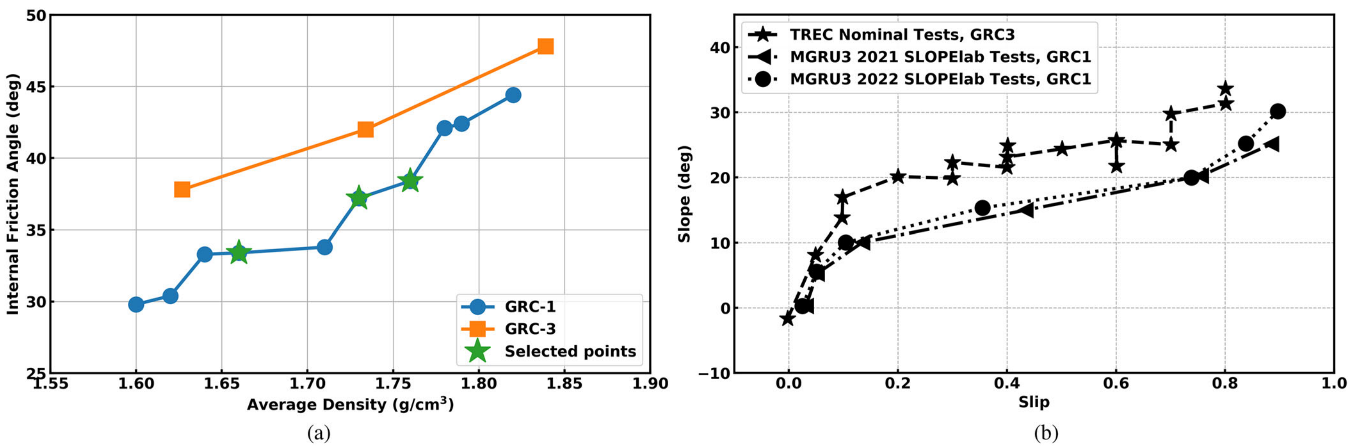

FIGURE 4 | Properties of GRC-1/GRC-3 lunar soil simulant and experimental results obtained in NASA's SLOPE lab. (a) Properties of GRC-1 and GRC-3 lunar soil simulant and (b) experimental results in NASA's SLOPE lab. GRC, Glenn Research Center; MGRU3, Moon Gravitation Representative Unit 3; TREC, Traction and Excavation Capabilities. [Color figure can be viewed at wileyonlinelibrary.com]

black star markers. The corresponding digital twin was built according to the rig information shown in Figure 5. The total load acting onto the deformable lunar soil simulant was induced by a 17.5 kg mass, of which half came from the wheel, the other half coming from extra nonwheel mass added to account for a part of the chassis. The wheel was driven with a constant translational velocity $v = 0.2\,\mathrm{m/s}$ on the bed of lunar simulant. The angular velocity was controlled to yield a predefined slip value $s = 1 - \frac{v}{\omega r}$, where $\omega > 0$ is the angular velocity and r is the effective radius of the wheel. Given a slip ratio s, in VV-mode, the wheel angular velocity was set to $\omega = \frac{v}{r(1-s)}$.

Each simulation was run for approximately 20 s with a slip s fixed at a predefined value in the 0–0.8 range. The ensuing average DBP force was measured as the force needed to be impressed at the wheel center to achieve this controlled VV-mode wheel movement. The simulation results are given in Figure 6, and when compared with the TREC experimental data (see the black-star markers in Figure 4b) they show good agreement for both the DBP versus slip and traction slope versus slip relationships. It is noted that each of the markers shown in the plot requires one complete 20 s simulation since the DBP force is an averaged value once the regime enters a steady state (the time histories of the DBP force for each slip ratio considered are shown in Figure 7). In these simulations, three different sets of GRC-3 material properties associated with the lunar soil simulant were chosen—with bulk densities 1627, 1734, and 1839 $\mathrm{kg/m^3}$, and internal friction angles 37.8°, 42.0°, and 47.8°, respectively, see Figure 4a to place these values in context.

Two salient points associated with this simulator validation test are as follows: (i) the physics-based simulator produces results in line with physical test results and (ii) it is more convenient to use a physics-based simulator, compared with a BWJH-class model. For the latter, one cannot use intuitive and relatively readily available gravity-independent parameters, such as bulk density and friction angle; rather, a bevameter test is required to identify the model parameters. Note that the outcomes of the bevameter test are gravity dependent—Moon parameters would require testing in Moon conditions.

3.2 | Slope-Mode: VIPER and Corresponding Single-Wheel Tests

This subsection presents results that highlight the following two aspects demonstrated via CRM terramechanics: there is no need to modify the mass or topology of the rover to predict through Earth tests the slope versus slip map or the power draw experienced by the rover while operating on the Moon in steady-state conditions; and results obtained for a single-wheel test are indicative of full-rover behavior.

In slope-mode, the rover was placed on a tilted terrain with an actual slope varied from $\theta = 0°$ to $30°$ $\theta = 30°$. As such, the gravitational pull might not be perpendicular to the terrain surface, which has implications in relation to the strength attributes of the soil. In these experiments, the wheels of the rover were driven with a constant angular velocity $\omega = 0.8\,\mathrm{rad/s}$; the translational velocity up the incline was not controlled—it was an outcome of the experiment. The MGRU3 results are shown in Figure 4b with circle and triangle markers.

Information about the slope-mode experiments is provided in Figure 8. For the simulations performed on GRC-1 simulant, there were $6 \times 3 \times 7 = 126$ simulations run: six red “check

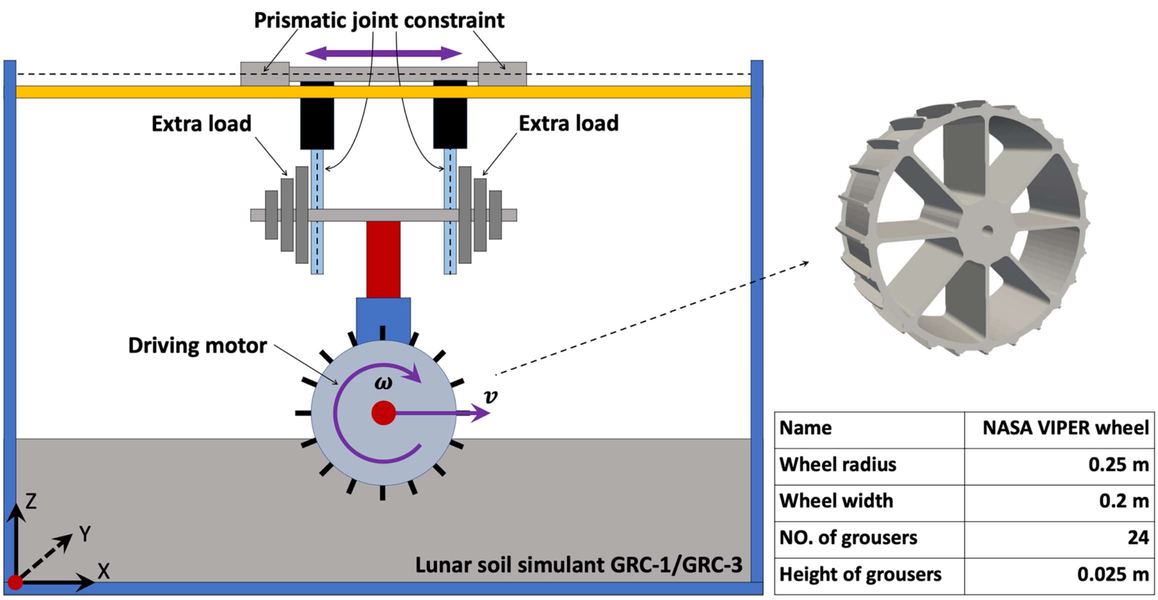

Name	NASA VIPER wheel
Wheel radius	0.25 m
Wheel width	0.2 m
NO. of grousers	24
Height of grousers	0.025 m

FIGURE 5 | Schematic view of the single-wheel test under velocity control mode (VV-mode). Both translational velocity and angular velocity of the wheel can be controlled using the test rig modeled in Chrono. Excess mass can be added on the wheel assembly to model wheel–soil interaction under various loads. The wheel used in the simulation shown here has the geometry used in NASA's SLOPE lab—the radius is 0.25 m, the width is 0.2 m, and there are 24 grousers. The height of each grouser is 0.025 m. GRC, Glenn Research Center; VIPER, Volatiles Investigating Polar Exploration Rover. [Color figure can be viewed at wileyonlinelibrary.com]

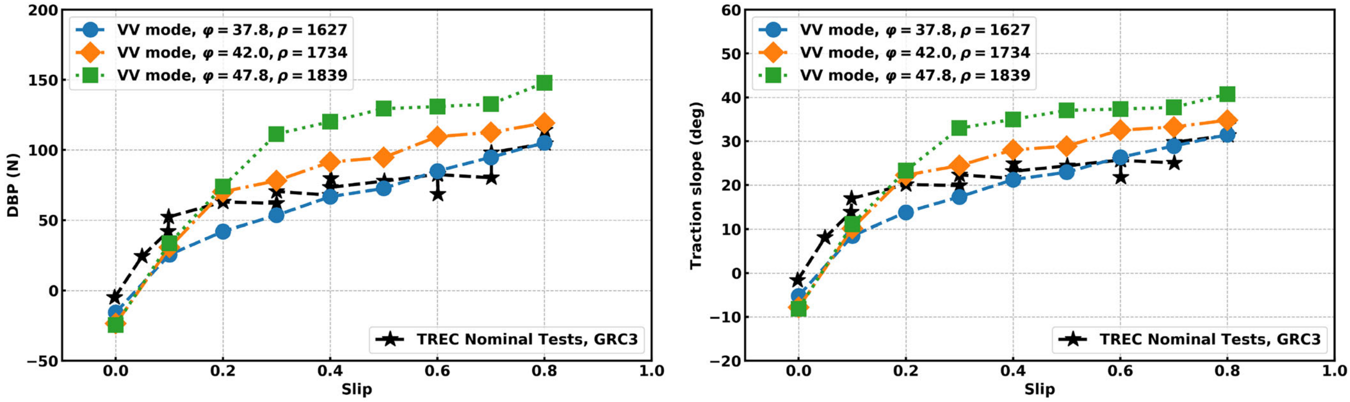

(a) (b)

FIGURE 6 | Single-wheel physical testing and simulation results on GRC-3 (He et al. 2013) lunar soil simulant using the 17.5 kg single-wheel test rig. Tests were performed under VV-mode. In simulation, three different sets of GRC-3 material properties associated with the lunar soil simulant were chosen—with bulk densities 1627, 1734, and 1839 kg/m^3, and internal friction angles 37.8°, 42.0°, and 47.8°, respectively. In these and all subsequent images, curves listed with black lines and markers correspond to *experimental* data, while curves listed with colored markers correspond to *simulation* data. The experimental data are connected with a dotted line to emphasize the physical measurements, which can at times be hard to discern against the simulation results. *Note:* that the experimental measurements might list multiple results for the same experimental setup, reflecting the uncertainty in physical measurements. (a) DBP versus slip and (b) traction slope versus slip. DBP, DrawBar-Pull; GRC, Glenn Research Center. [Color figure can be viewed at wileyonlinelibrary.com]

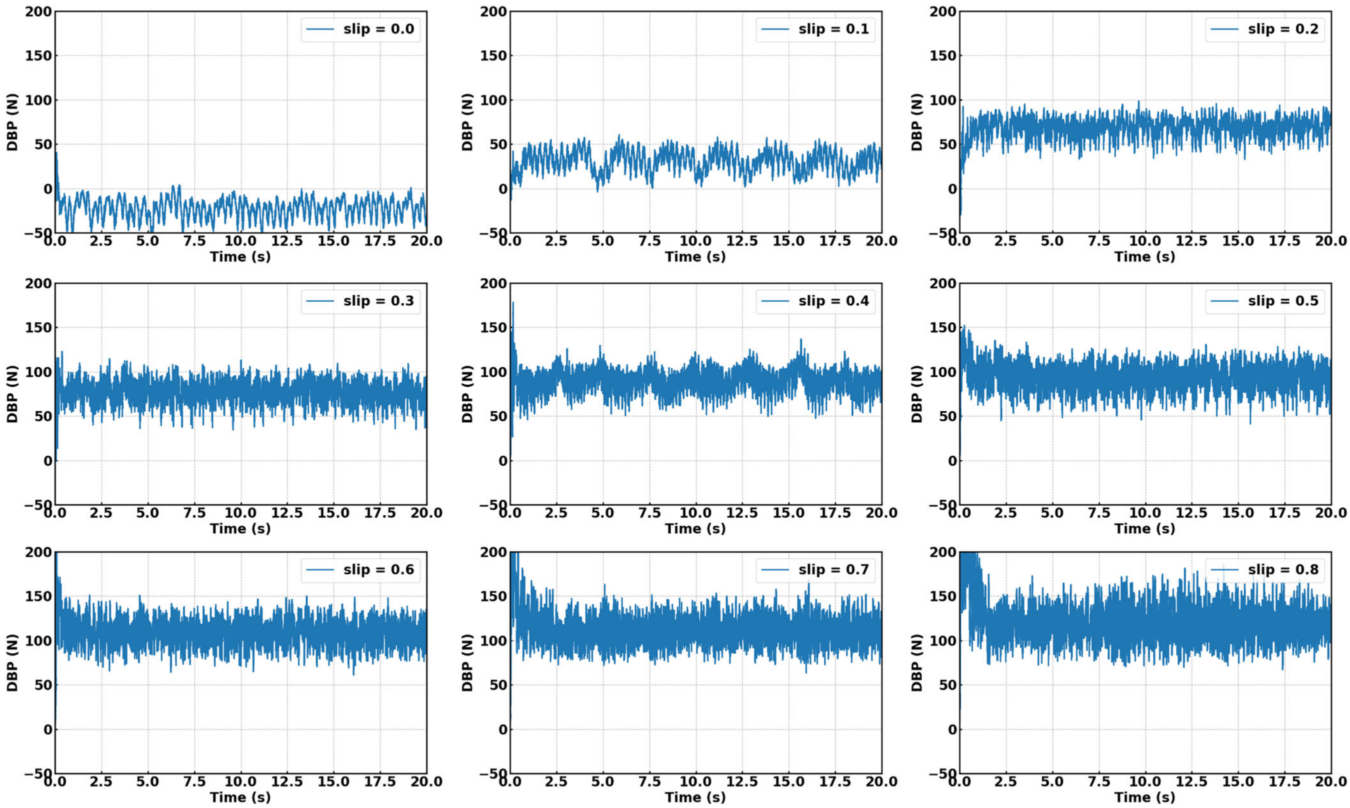

FIGURE 7 | Time history of DBP force measured on the wheel at each slip ratio. The simulations were performed on GRC-3 lunar soil simulant in VV-mode. Steady state can be observed in each of the experiments. *Note:* that at zero slip, the force is negative. The density and internal friction angle were 1734 kg/m^3 and 42.0°, respectively. DBP, DrawBar-Pull; GRC, Glenn Research Center. [Color figure can be viewed at wileyonlinelibrary.com]

marks" in Figure 8; three angular velocities—$\omega = 0.8$ rad/s for Earth, and $\omega = 0.33$ and 0.8 rad/s for the Moon; and seven slopes, $\theta = 0°, 5°, 10°, 15°, 20°, 25°, 30°$. Each simulation ran for approximately 20 s to ensure that a steady state was reached. At steady state, we measured the average rover translational velocity v and subsequently calculated the associated slip ratio s. To investigate whether single-wheel results are indicative of full-rover dynamics, we also ran the single-wheel simulation in the

Properties of Lunar Soil Simulant (Unit: kg/m³, deg)		Single Wheel		Full Rover	
		17.5 kg	22 kg	73 kg	88 kg
GRC-3	$\rho = 1627, \varphi = 37.8$	✓		✓	
	$\rho = 1734, \varphi = 42.0$	✓		✓	
	$\rho = 1839, \varphi = 47.8$	✓		✓	
GRC-1	$\rho = 1660, \varphi = 33.4$		✓		✓
	$\rho = 1730, \varphi = 37.2$		✓		✓
	$\rho = 1760, \varphi = 38.4$		✓		✓

FIGURE 8 | The summary of "slope-mode" simulation cases. Three different sets of material properties (density and friction angle) of GRC-3 and GRC-1 were used. The simulations were run under both Earth gravity and Moon gravity. Two different angular velocities (0.8 and 0.33 rad/s) were used in the simulations under Moon gravity to assess the extent to which the simulation results come in line with the granular scaling laws. GRC, Glenn Research Center. [Color figure can be viewed at wileyonlinelibrary.com]

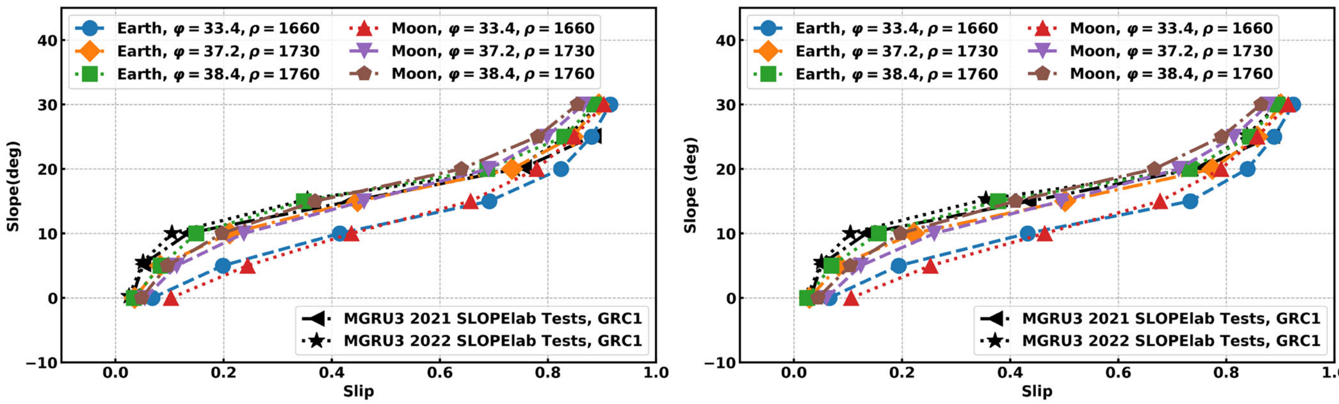

(a) (b)

FIGURE 9 | Single-wheel and full-rover simulation using CRM on GRC-1 lunar soil simulant. Curves listed with black lines and markers correspond to *experimental* data, while curves listed with colored markers correspond to *simulation* data. A 22 kg single-wheel test rig and 88 kg MGRU3 rover were used in the simulations. The wheel angular velocity was set to 0.8 rad/s in the simulations with Earth gravity, and 0.33 rad/s for Moon gravity according to the granular scaling laws discussed in Zhang et al. (2020). All the values used to generate the markers in the figures were averaged out in steady state for each slope scenario. In the slope-mode plots, one would start with a slope on the y-axis and *Note:*the slip it led to on the x-axis. (a) Single wheel on GRC-1 and (b) full rover on GRC-1. CRM, continuous representation model; GRC, Glenn Research Center; MGRU3, Moon Gravitation Representative Unit 3.

same slope-mode with approximately 1/4 of the mass of the rover. The densities of GRC-1 used in the CRM simulation were 1660, 1730, and 1760 kg/m^3. The internal friction angles were 33.4°, 37.2°, and 38.4°, respectively; see Figure 4a for placing these values in context. To be consistent with the experimental data obtained from the NASA's TREC test rig for single wheel and the MGRU3 for the full VIPER, an 88 kg digital twin was built in the GRC-1 scenarios. In the single-wheel test, a 22 kg (which is 88/4) wheel was used, in accordance with how MGRU3's mass changed during the design phase of VIPER. Under Moon gravity, we considered an angular velocity $\omega = 0.33\,\text{rad/s}$ since this is roughly $\frac{1}{\sqrt{6}}$ of the value used under Earth gravity. This ratio is dictated by the scaling law (outlined in Zhang et al. 2020) as the one necessary to predict the rover's performance on the Moon.

Figure 9 compares simulation results and the experimental data under both Earth and Moon gravity. The salient points are as follows: (i) the single-wheel and full-rover simulations performed under Earth gravity match well the physical test results obtained at SLOPE lab and (ii) the rover's performance on the Moon is consistent with that observed on Earth in terms of the slope/slip relationship if the wheel driving angular velocity meets the requirement according to scaling law reported in Zhang et al. (2020).

The results illustrated in Figures 10 and 11 were used to generate the green and brown curves in Figure 9a,b. Specifically, GRC-1 simulations with a bulk density of 1760 kg/m^3 and friction angle 38.4° were run for θ between 0° and 30° in increments of 5°—under Earth gravity in Figure 11a and Moon gravity in Figure 11b. Each slope θ leads to a velocity profile in Figure 11a, and that velocity profile, when averaged out at steady state, leads to a slip value, which represents one dot on the green line in Figure 9b. Likewise, each θ leads to a lunar velocity profile in Figure 11b, and that velocity profile, when averaged out at steady state leads to a slip value, which represents one dot on the brown line in Figure 9b. Note how the scaling law emerges from the results reported in Figure 11: for instance, when the slope of the terrain was 15° (red lines in the plots), on the left, the rover average velocity on Earth was approximately 0.125 m/s; in Moon gravity, the speed averaged at 0.05 m/s. The ratio between these numbers works out to be

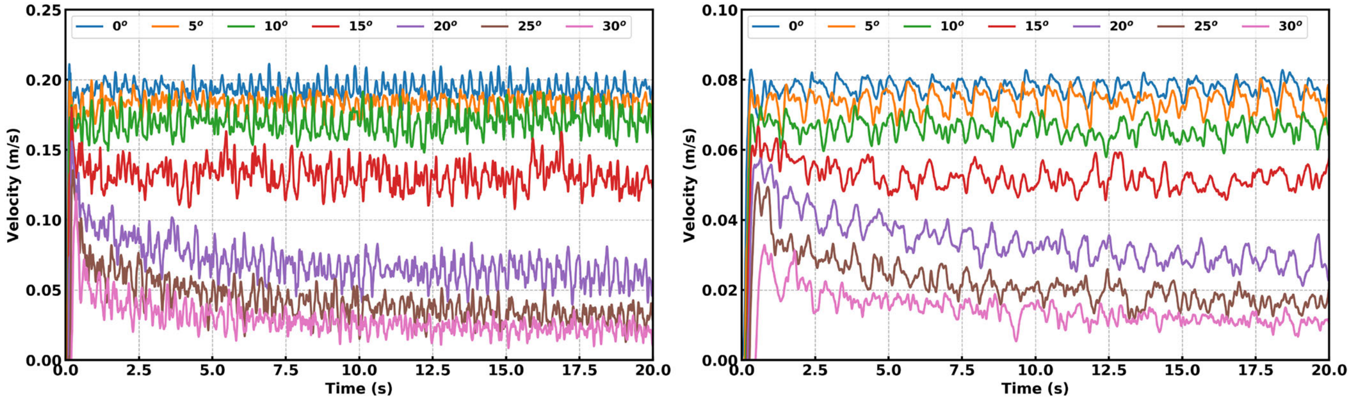

(a) (b)

FIGURE 10 | Time history of translational velocity of single-wheel simulation on GRC-1. Tests were done for terrain slopes between 0° and 30° in increments of 5° with a bulk density of 1760 kg/m^3 and friction angle 38.4°. The information in these two plots was used to generate the green and brown curves in Figure 9a. (a) Earth gravity with $\omega = 0.8$ rad/s and (b) Moon gravity with $\omega = 0.33$ rad/s. GRC, Glenn Research Center. [Color figure can be viewed at wileyonlinelibrary.com]

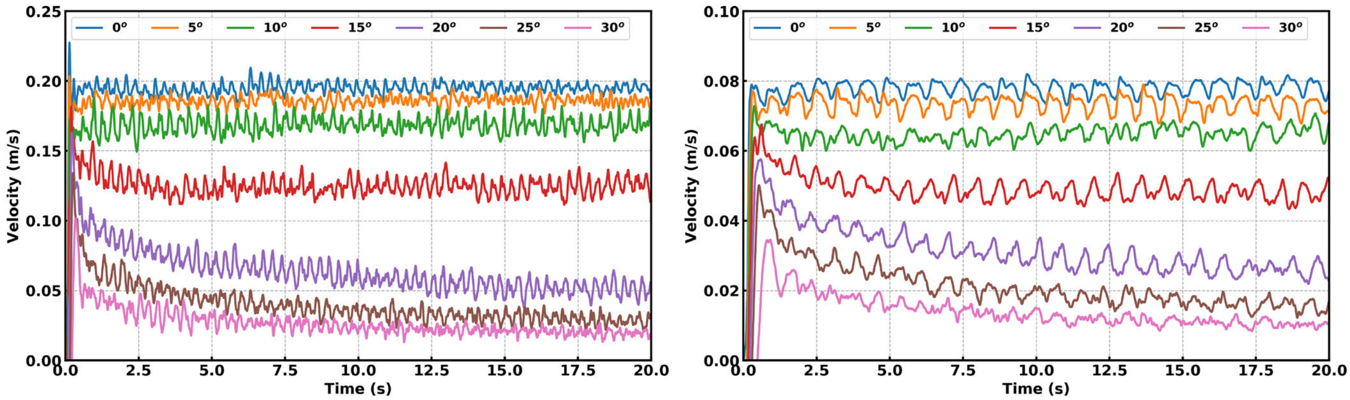

(a) (b)

FIGURE 11 | Time history for MGRU3's velocity simulated on GRC-1. Tests were done for terrain slopes between 0° and 30° in increments of 5° with a bulk density of 1760 kg/m^3 and friction angle 38.4°. The information in these two plots was used to generate the green and brown curves in Figure 9b. (a) Earth gravity, angular velocity $\omega = 0.8$ rad/s and (b) Moon gravity, angular velocity $\omega = 0.33$ rad/s. GRC, Glenn Research Center; MGRU3, Moon Gravitation Representative Unit 3. [Color figure can be viewed at wileyonlinelibrary.com]

approximately $\sqrt{6}$. The same $\sqrt{6}$ ratio holds if one compares any two curves of identical color in the left and right plots in Figure 11.

Figure 12 reports single-wheel and full-rover simulation results on GRC-1 simulant under Earth and Moon gravity. In this case, the single-wheel simulation closely predicted the full vehicle performance. In general, running single-wheel simulations can be used as a good approximation for full vehicle performance but the fidelity of the predictions is vehicle dependent. Specifically, a single-wheel test is a good proxy for full vehicle performance for steady-state regimes, for example, vehicle moving on planar surfaces, moving straight up on a steady incline. For active suspension cases or whenever the wheel load becomes complex and time dependent, one is forced to work with the full vehicle since subtle load transfer scenarios come into play when the vehicle moves through negative or positive obstacles, engages in slope banking maneuvers, performs U-turns on sloped areas, and so forth. Note that the single-wheel simulation is approximately four times faster due to the fewer SPH particles that participate in the CRM simulation. This is accomplished by using "active domains"—only the dynamics of the material in the proximity of the implements that come in contact with the soil, that is, the active domain, is simulated rather than the terramechanics of the entire mass of regolith.

To gain insights into how the mobility attributes change with the angular velocity, a set of single-wheel and full-rover simulations were run under Moon gravity with a higher angular velocity $\omega = 0.8$ rad/s; a comparison with results obtained for $\omega = 0.33$ rad/s is provided in Figure 13. The results are almost identical, as up to a critical value of the angular velocity, the slope/slip relationship is not sensitive to angular velocity (see Figure 3A in Agarwal et al. 2021). Note, however, that should one look at the translational velocity of the lunar rover at $\omega = 0.8$ rad/s, the scaling law would not be able to correlate that translational velocity to the one of the rover moving on Earth when the wheels are driven at $\omega = 0.8$ rad/s.

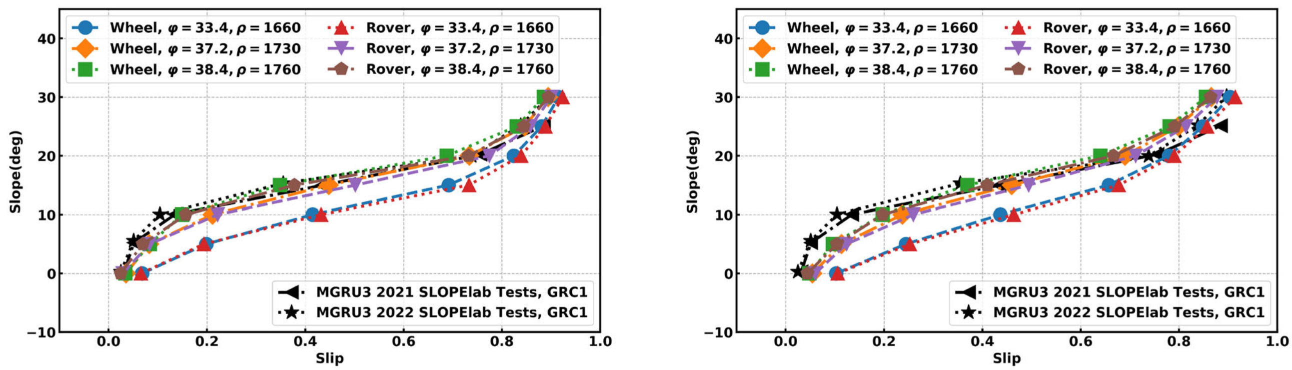

(a) (b)

FIGURE 12 | A comparison between single-wheel and MGRU3 simulations using GRC-1 lunar soil simulant with both Earth and Moon gravity. *Note:* that single-wheel performance is indicative of full-rover performance. Curves listed with black lines and markers correspond to *experimental* data, while curves listed with colored markers correspond to *simulation* data. (a) Single-wheel versus full-rover results—Earth gravity on GRC-1, $\omega = 0.8$ rad/s and (b) single-wheel versus full-rover results—Moon gravity on GRC-1, $\omega = 0.33$ rad/s. GRC, Glenn Research Center; MGRU3, Moon Gravitation Representative Unit 3. [Color figure can be viewed at wileyonlinelibrary.com]

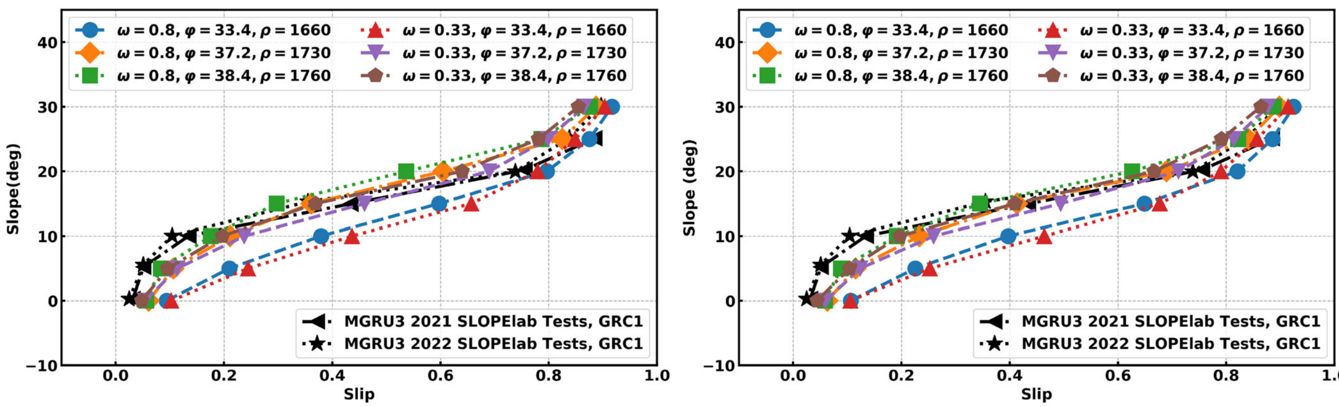

(a) (b)

FIGURE 13 | Single-wheel and full-rover simulation using on GRC-1 lunar soil simulant *under Moon gravity*. Two different angular velocities were used—0.33 and 0.8 rad/s, yet the slope versus slip curves are identical. Curves listed with black lines and markers correspond to *experimental* data, while curves listed with colored markers correspond to *simulation* data. (a) Single wheel on GRC-1 and (b) full rover on GRC-1. GRC, Glenn Research Center; MGRU3, Moon Gravitation Representative Unit 3. [Color figure can be viewed at wileyonlinelibrary.com]

Figure 14 gives the *scaled* power/slip relationship for two scenarios: single wheel and full rover on GRC-1 lunar soil simulant, where the *scaled* power $\frac{P}{Mg\sqrt{Lg}}$ is the term on the left-hand side of Equation (1). One angular velocity 0.8 rad/s was used in the simulations under Earth gravity, while two different angular velocities, 0.33 and 0.8 rad/s, were used in the simulations under Moon gravity. Note that if the angular velocity in the Earth experiment is roughly $\sqrt{6}$ times larger than that used under Moon gravity, the *scaled* powers are identical. If we use the same angular velocity to do the tests on both Moon and Earth, there will be a gap between these two sets of simulations for both single wheel and full rover, as shown in Figure 14b,d. The results indicate that the *scaled* power/slip relationship obtained in simulation produces results predicted by the GSL (Zhang et al. 2020).

To demonstrate the conclusion we reported in the GRC-1 simulations, we performed similar simulations on GRC-3 for both single wheel (17.5 kg, which is roughly 1/4 of the mass of the rover) and full VIPER rover (73 kg). Information about the slope-mode experiments is provided in Figure 8. There were $6 \times 3 \times 7 = 126$ simulations run: six red "check marks" in Figure 8; three angular velocities—$\omega = 0.8$ rad/s for Earth, and $\omega = 0.33$ and 0.8 rad/s for the Moon; and seven slopes, $\theta = 0°, 5°, 10°, 15°, 20°, 25°, 30°$. Each simulation ran for approximately 20 s to ensure that a steady state was reached. At steady state, we measured the average rover translational velocity v and subsequently calculated the associated slip ratio s. The densities of GRC-3 used in the CRM simulation were 1627, 1734, and 1839 kg/m^3. The internal friction angles were 37.8°, 42.0°, and 47.8°, respectively; see Figure 4a for placing these values in context. Under Moon gravity, we considered an angular velocity $\omega = 0.33$ rad/s since this is roughly $\frac{1}{\sqrt{6}}$ of the value used under Earth gravity. This ratio is dictated by the scaling law (outlined in Zhang et al. 2020) as the one necessary to predict the rover's performance on the Moon. The corresponding simulation results are shown in Figures 15–20.

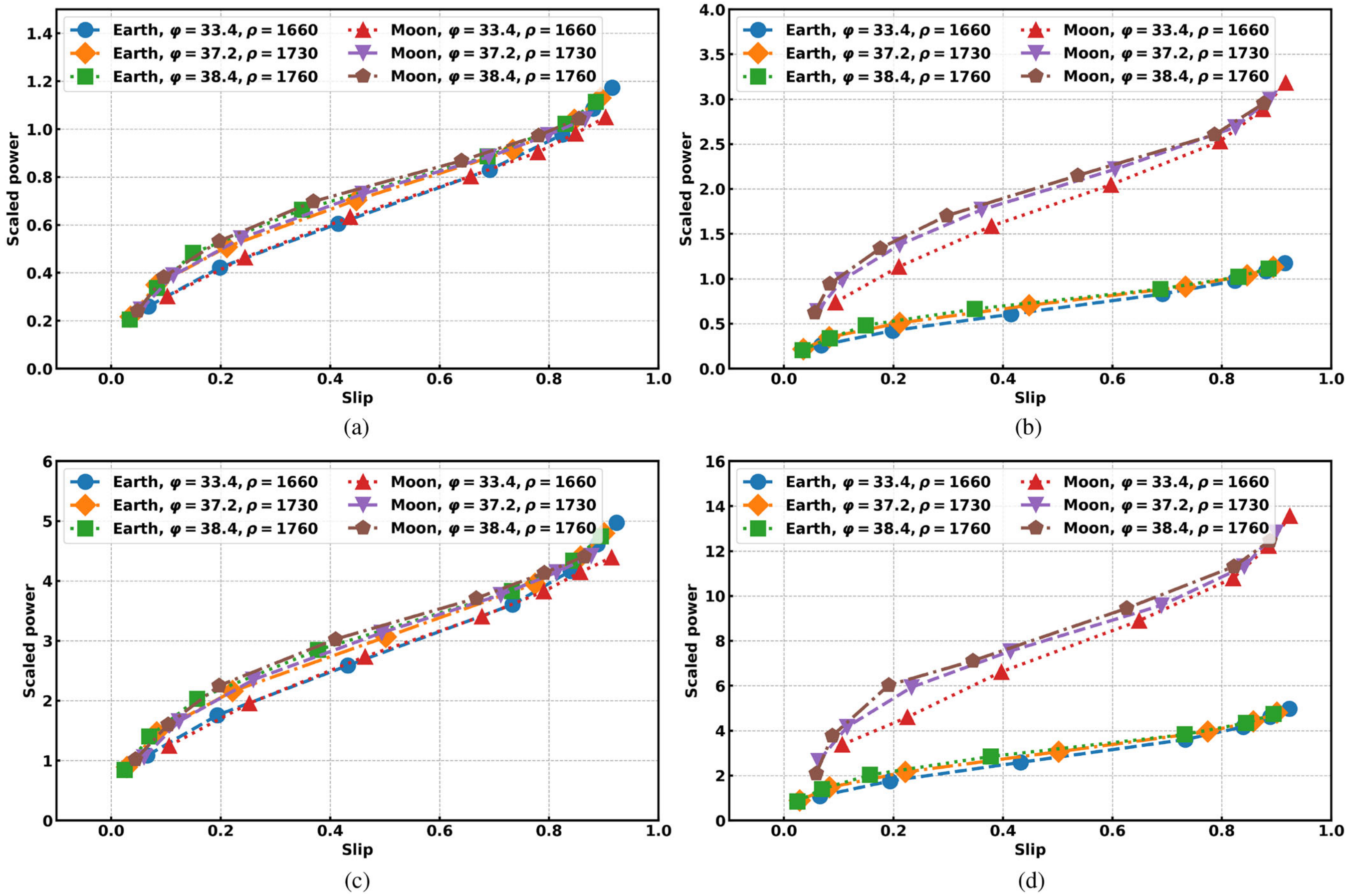

FIGURE 14 | Scaled wheel power at steady state of single-wheel/full-rover simulation using CRM on GRC-1 lunar soil simulant. The scaled powers are identical if the angular velocity in the Earth experiment is roughly $\sqrt{6}$ times larger than that used under Moon gravity. The scaled powers show a large gap if the same angular velocity is used for tests on Moon and Earth. (a) Single wheel: $\omega = 0.8$ rad/s on Earth, $\omega = 0.33$ rad/s on Moon, (b) single wheel: $\omega = 0.8$ rad/s on Earth, $\omega = 0.8$ rad/s on Moon, (c) full rover: $\omega = 0.8$ rad/s on Earth, $\omega = 0.33$ rad/s on Moon, and (d) full rover: $\omega = 0.8$ rad/s on Earth, $\omega = 0.8$ rad/s on Moon. CRM, continuous representation model; GRC, Glenn Research Center. [Color figure can be viewed at wileyonlinelibrary.com]

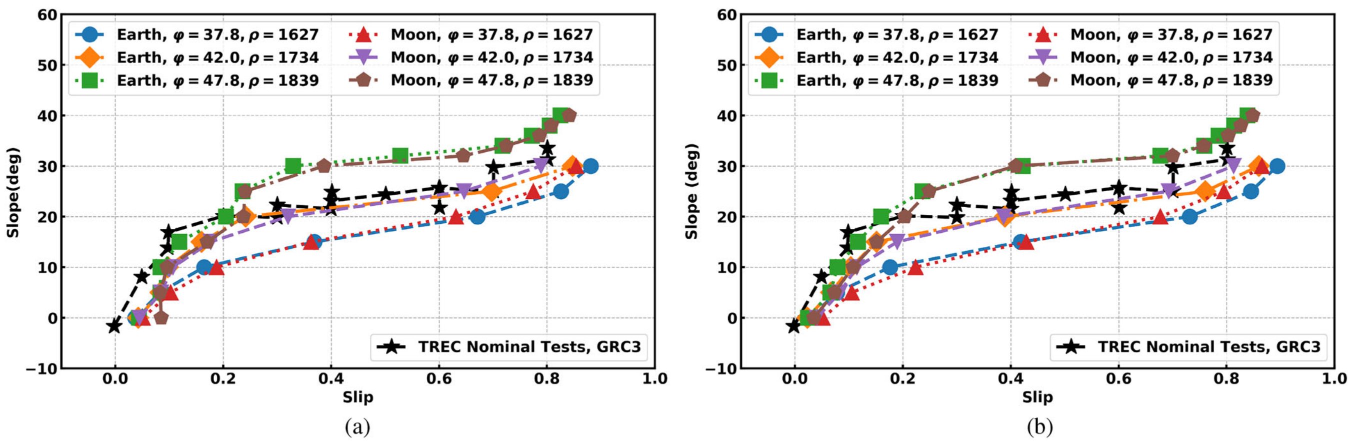

FIGURE 15 | Single-wheel and full-rover simulation using CRM on GRC-3 lunar soil simulant. Curves listed with black lines and markers correspond to *experimental* data, while curves listed with colored markers correspond to *simulation* data. A 17.5 kg single-wheel test rig and 73 kg MGRU3 rover were used in the simulations on GRC-3. The wheel angular velocity was fixed to 0.8 rad/s in the simulations with Earth gravity, while fixed to 0.33 rad/s in the ones with Moon gravity according to the scaling law (Zhang et al. 2020). All the values used to generate the markers in the figures were obtained in steady state for each individual slip scenario. The single-wheel results were obtained in the TREC Rig at Glenn Research Center. (a) Single wheel on GRC-3 and (b) full rover on GRC-3. CRM, continuous representation model; GRC, Glenn Research Center; MGRU3, Moon Gravitation Representative Unit 3; TREC, Traction and Excavation Capabilities. [Color figure can be viewed at wileyonlinelibrary.com]

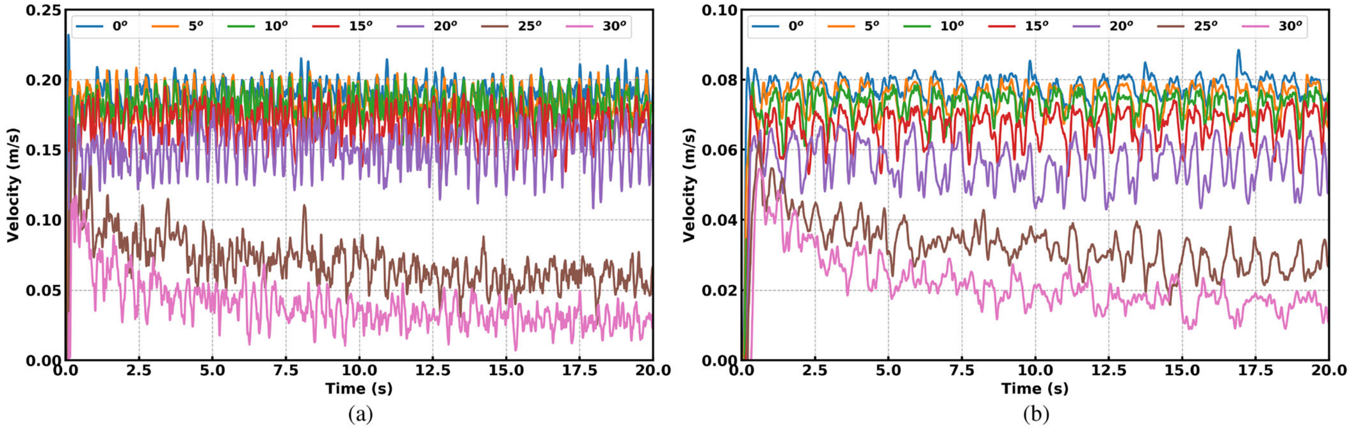

FIGURE 16 | Time history of translational velocity of single-wheel simulation on GRC-3. Tests were done for terrain slopes between 0° and 30° in increments of 5° with a bulk density of 1734 kg/m^3 and friction angle 42.0°. The information in these two plots was used to generate the yellow and purple curves in Figure 15a. (a) Earth gravity with $\omega = 0.8$ rad/s and (b) Moon gravity with $\omega = 0.33$ rad/s. GRC, Glenn Research Center. [Color figure can be viewed at wileyonlinelibrary.com]

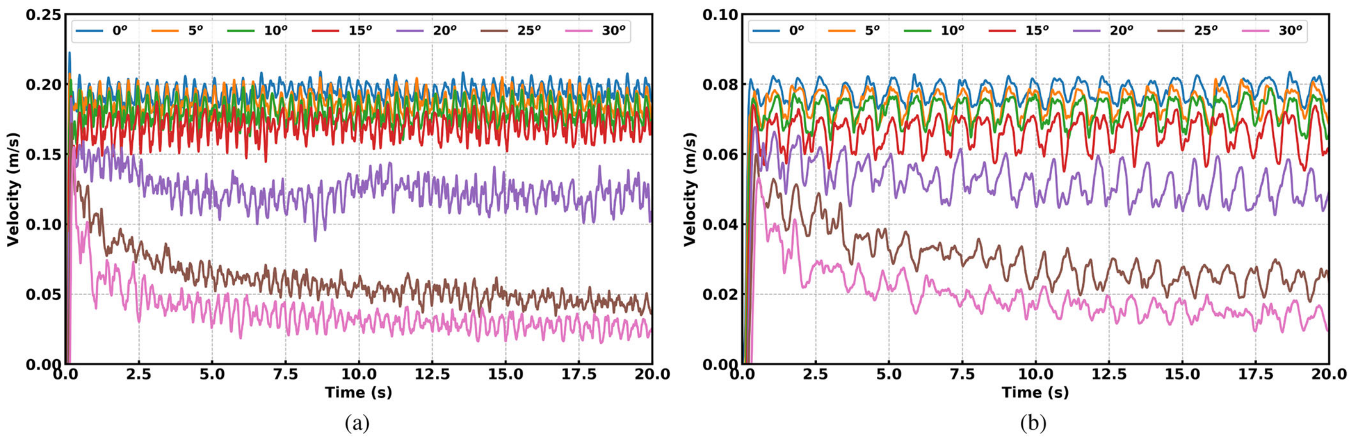

FIGURE 17 | Time history of translational velocity of full rover on GRC-3. Tests were done for terrain slopes between 0° and 30° in increments of 5° with a bulk density of 1734 kg/m^3 and friction angle 42.0°. The information in these two plots was used to generate the yellow and purple curves in Figure 15b. (a) Earth gravity with $\omega = 0.8$ rad/s and (b) Moon gravity with $\omega = 0.33$ rad/s. GRC, Glenn Research Center. [Color figure can be viewed at wileyonlinelibrary.com]

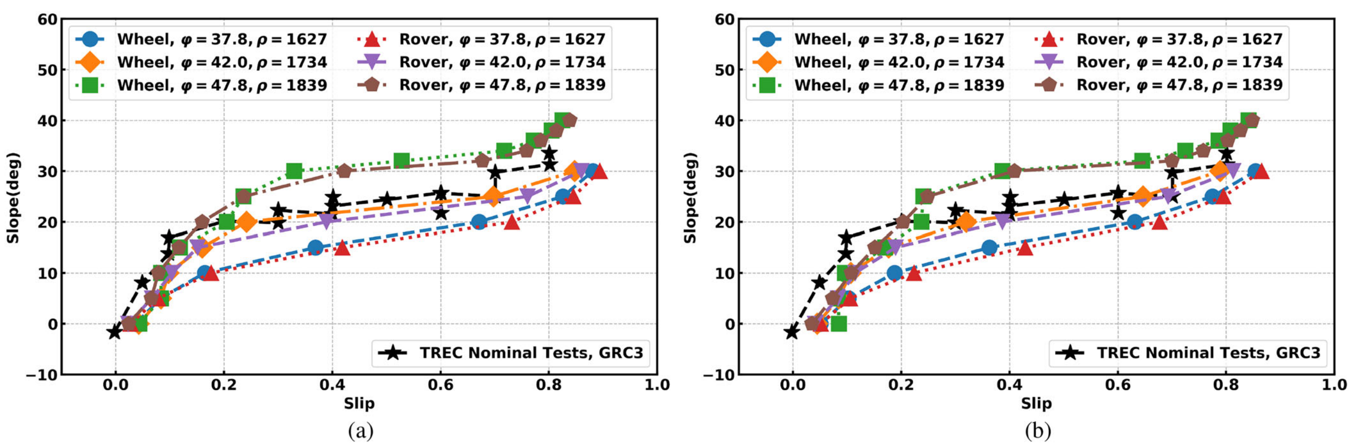

FIGURE 18 | A comparison between single-wheel and MGRU3 simulations using GRC-3 lunar soil simulant with both Earth and Moon gravity. Curves listed with black lines and markers correspond to *experimental* data, while curves listed with colored markers correspond to *simulation* data. (a) Earth gravity on GRC-3 and (b) Moon gravity on GRC-3. GRC, Glenn Research Center; MGRU3, Moon Gravitation Representative Unit 3. [Color figure can be viewed at wileyonlinelibrary.com]

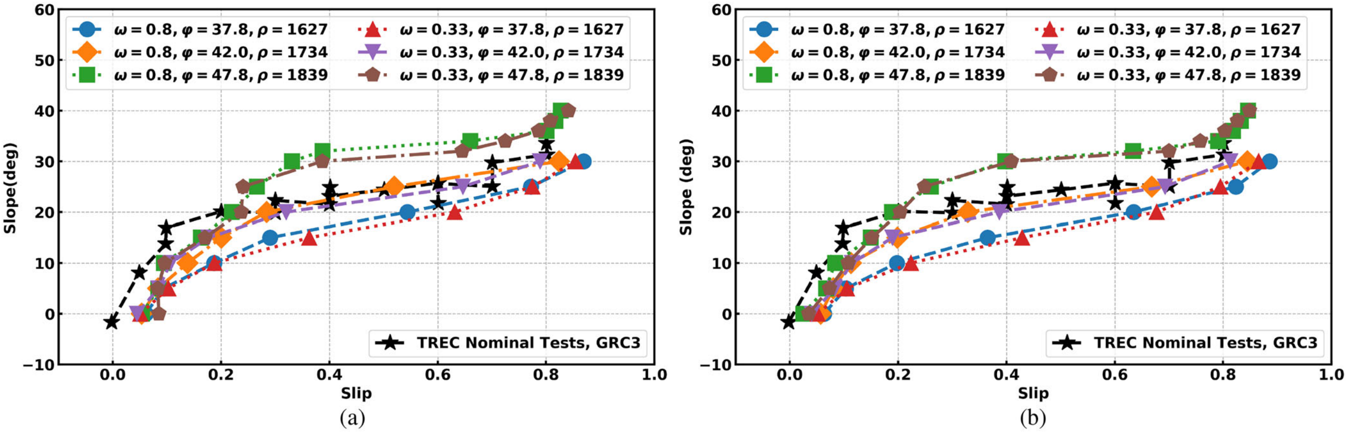

FIGURE 19 | Single-wheel and full VIPER rover simulation using on GRC-3 lunar soil simulant under Moon gravity. Two different angular velocities were used—0.33 and 0.8 rad/s. Curves listed with black lines and markers correspond to *experimental* data, while curves listed with colored markers correspond to *simulation* data. (a) Single wheel on GRC-3 and (b) full rover on GRC-3. GRC, Glenn Research Center; TREC, Traction and Excavation Capabilities; VIPER, Volatiles Investigating Polar Exploration Rover. [Color figure can be viewed at wileyonlinelibrary.com]

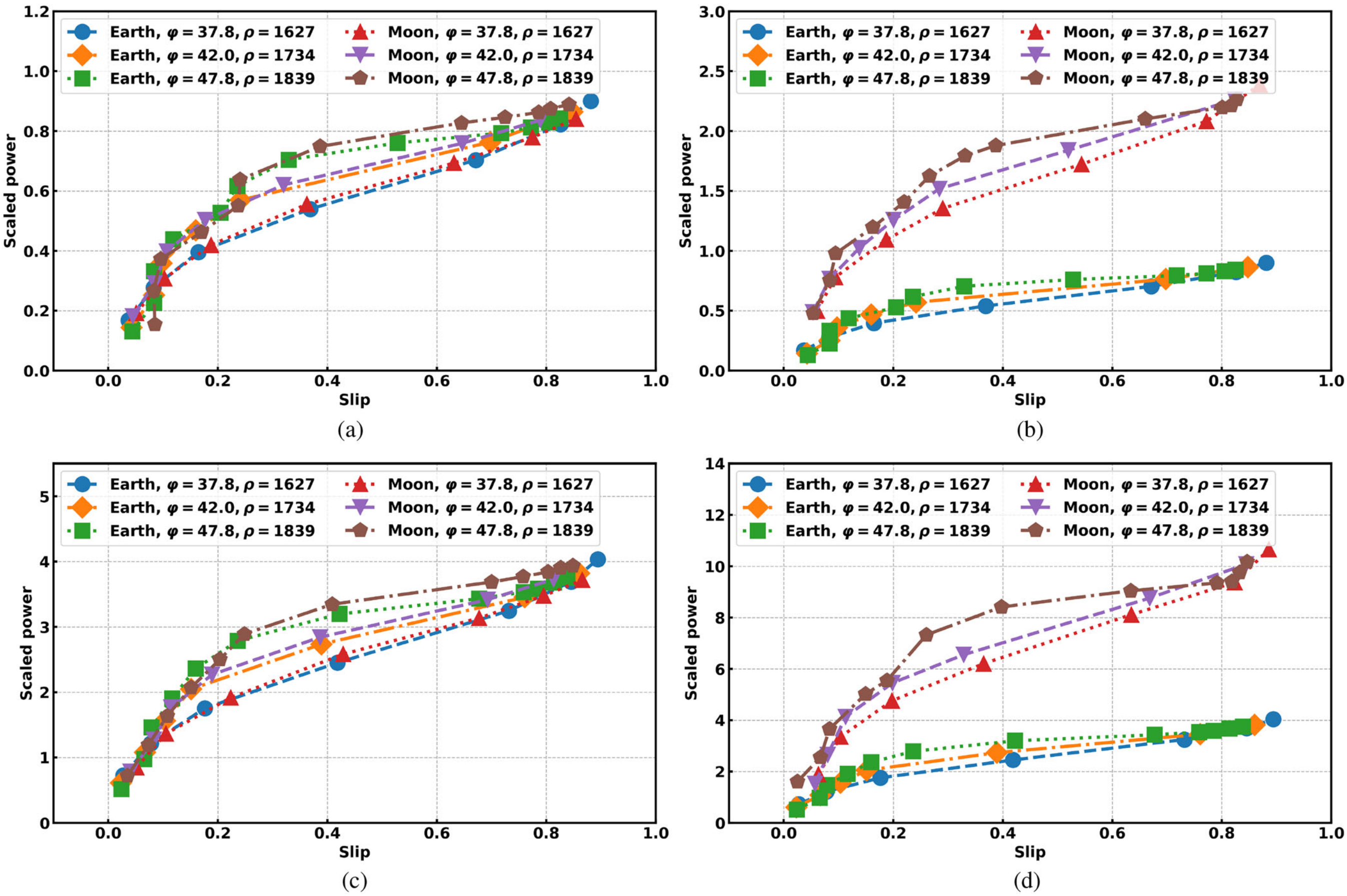

FIGURE 20 | Scaled wheel power at steady state of single-wheel/full-rover simulation using CRM on GRC-3 lunar soil simulant. The scaled powers are identical if the angular velocity in the Earth experiment is roughly $\sqrt{6}$ times larger than that used under Moon gravity. The scaled powers show a large gap if the same angular velocity is used for tests on Moon and Earth. (a) Single wheel: $\omega = 0.8$ rad/s on Earth, $\omega = 0.33$ rad/s on Moon, (b) single wheel: $\omega = 0.8$ rad/s on Earth, $\omega = 0.8$ rad/s on Moon, (c) full rover: $\omega = 0.8$ rad/s on Earth, $\omega = 0.33$ rad/s on Moon, and (d) full rover: $\omega = 0.8$ rad/s on Earth, $\omega = 0.8$ rad/s on Moon. CRM, continuous representation model; GRC, Glenn Research Center. [Color figure can be viewed at wileyonlinelibrary.com]

The conclusions for the GRC-3 simulations are as follows: (i) the single-wheel and full-rover simulations performed under Earth gravity match well the physical test results obtained at SLOPE lab, (ii) the rover's performance on the Moon is consistent with that observed on Earth in terms of the slope/slip relationship if the wheel driving angular velocity meets the requirement according to scaling law reported in Zhang et al. (2020), and (iii) if the angular velocity in the Earth experiment

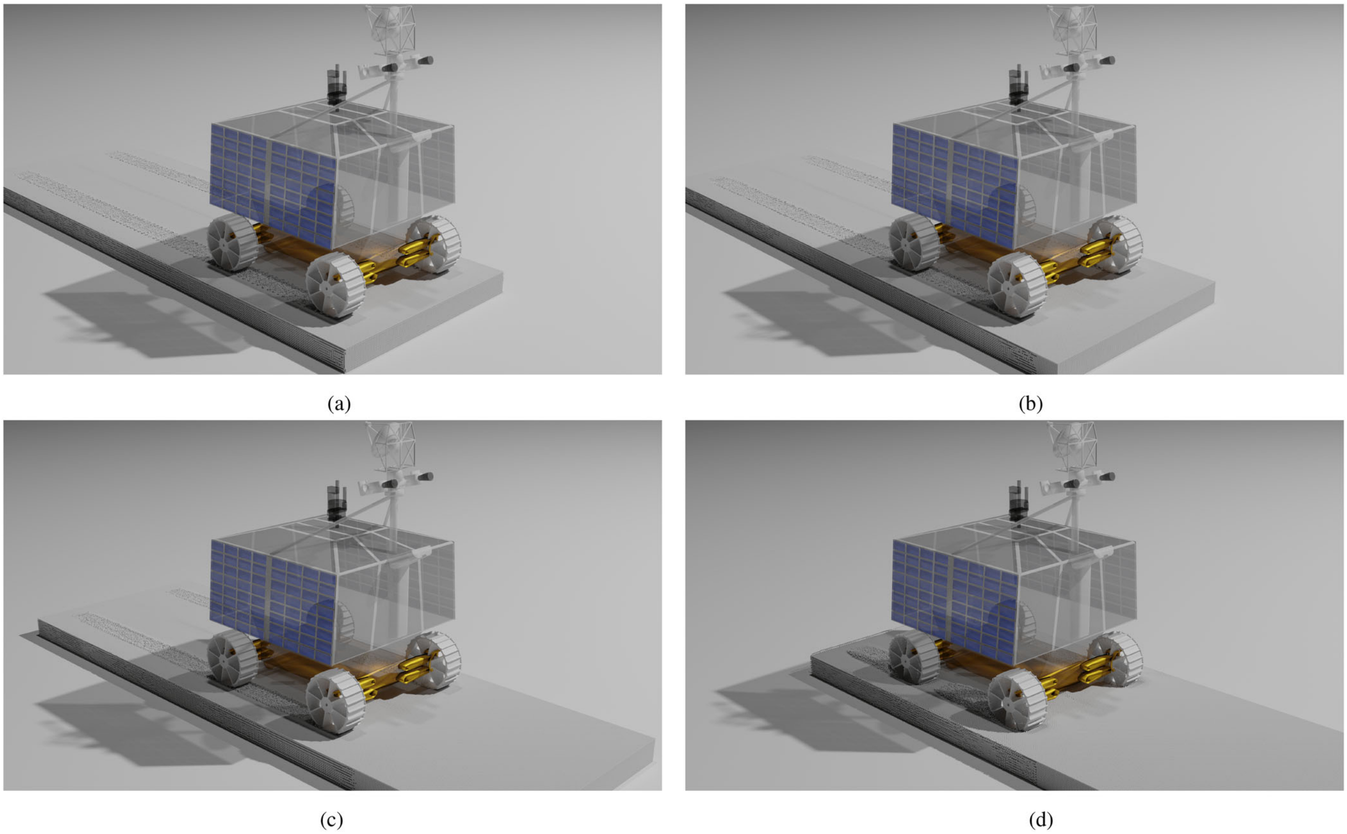

FIGURE 21 | Screenshots of the 73 kg rover simulated on GRC-3 under Earth gravity, 20 s into the motion of the rover. The terrain slope is accounted for by changing the direction of the gravitational pull. (a) Slope = 0°, (b) slope = 10°, (c) slope = 20°, and (d) slope = 30°. GRC, Glenn Research Center. [Color figure can be viewed at wileyonlinelibrary.com]

is roughly $\sqrt{6}$ times larger than that used under Moon gravity, the *scaled* powers are identical, if we use the same angular velocity to do the tests, there will be a gap between these two sets of simulations for both single wheel and full rover, as shown in Figure 20b,d.

Figure 21 shows screen shots of the 73 kg rover moving over GRC-3 lunar soil simulant at several terrain slopes θ, between 0° and 30°. The angular velocity at the wheel was $\omega = 0.8\,\text{rad/s}$; the GRC-3 density and internal friction angle were 1734 kg/m^3 and 42.0°, respectively. To compare the images, all terrains were rotated back with the terrain to be shown as horizontal. As expected, the higher the terrain slope, the shorter the distance the rover can move up the incline in a given amount of time, and the higher the wheel–soil sinkage.

4 | Discussion and Concluding Remarks

This manuscript summarizes lessons learned in a simulation campaign undertaken during the design phase of VIPER. Assessing the trafficability worthiness of the rover design was anchored by the methodology in use at NASA and currently embraced by other space agencies. At the onset of this study, VIPER's mass was approximately 440 kg (during the design phase, its mass increased from 440 to 520 kg due to instrumentation decisions). Since VIPER is Moon-bound, the MGRU3 scarecrow was built at a mass roughly 1/6 of the nominal rover's mass. This gravity-offload decision explains why the 2021–2022 physical testing results reported in Section 3 are for a *rover* with masses of 73 and 88 kg. These MGRU3 masses were used in the experimental campaign at the SLOPE lab to collect data and assess the mobility traits of the roughly 500 kg VIPER. Although this study drew on VIPER testing results and was meant to assess that rover's trafficability attributes, the lessons learned are relevant in the process of designing any wheeled or tracked rovers aimed to operate on the Moon, Mars, or other celestial bodies in low gravity. The conclusion of this study is that full-vehicle tests on Earth augmented with simulations and GSLs insights provide a framework that can anchor the design process of a vehicle operating in non-Earth gravitational fields.

Our results suggest that there was no need to keep the geometry of the rover yet reduce its mass. Indeed, the nominal vehicle produced the same slip versus slope curves on the Moon and on Earth. If one reduced the rover mass for Earth testing, a light rover would be placed on granular material acted upon by the Earth's gravitational pull, leading to overoptimistic performance for the nominal rover when deployed on a celestial body of lower gravity. GRC-1 and GRC-3 were intended to counterbalances this. The stated purpose of GRC-1 was to allow a lunar rover at 1/6 mass nominal mass to be tested on Earth to gauge performance of the nominal rover operating on the Moon. However, given that the friction angle and bulk densities of GRC-1 are similar to those of the lunar regolith (see Figure 4a), the terrain on Earth (under high gravitational pull) might have a higher shear yield point *and* have to support a lower-mass vehicle. This qualitative analysis has a quantitative counterpart

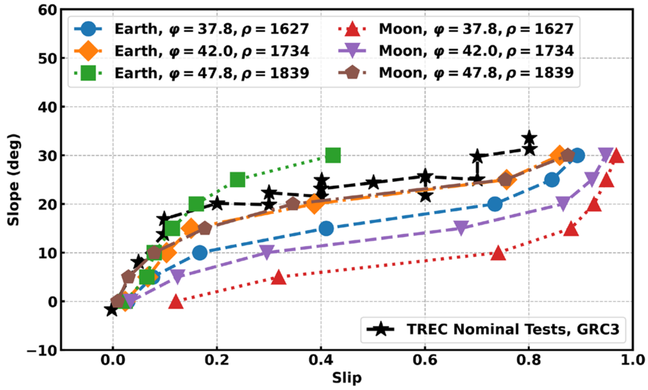

FIGURE 22 | Slope-mode analysis: physical testing data versus CRM simulation results for the MGRU3 rover on Earth, and VIPER rover on the Moon. The former rover has a mass of 73 kg, a reflection of the misconception that gravitational offset is necessary on Earth. The VIPER rover has a mass of 440 kg and is simulated in Moon gravity. Curves listed with black lines and markers correspond to *experimental* data, while curves listed with colored markers correspond to *simulation* data. The simulation results confirm that placing a light vehicle on terrain that has Earth-gravity induced higher strength leads to misleading results. CRM, continuous representation model; GRC, Glenn Research Center; MGRU3, Moon Gravitation Representative Unit 3; TREC, Traction and Excavation Capabilities; VIPER, Volatiles Investigating Polar Exploration Rover. [Color figure can be viewed at wileyonlinelibrary.com]

in Figure 22. The information captured therein is associated with slope-mode testing. The plot reports physical testing data versus CRM simulation results for the MGRU3 rover on Earth, and VIPER rover on the Moon. The former rover has a mass of 73 kg—a low mass value reflecting the common belief that gravitational offset is necessary on Earth. The VIPER rover has a mass of 440 kg and is simulated in Moon gravity. To argue that placing a light vehicle on terrain with Earth gravity-induced higher strength leads to optimistic results, consider the situation where the GRC-3 terrain has a friction angle $\phi = 47.8$ and bulk density $\rho = 1839$. On Earth, the results are associated with the line with green squares; on the Moon, this would be the line with brown pentagons. The results indicate that MGRU3 climbs a $\theta = 30°$ slope and it can do so at a slip value of approximately 42%. However, if the VIPER rover was to climb on the Moon a $\theta = 30°$ slope, it would experience significantly higher slip, approximately 85%. This is an example of over-optimistic results produced by Earth testing, as slip values above 80% would place the rover in a situation that increases the propensity for dig-in. The same optimistic behavior is noted for other friction angle and bulk density values. For instance, consider the $\phi = 37.8$ and $\rho = 1627$ GRC-3 case—blue circles on Earth for MGRU3, red triangles on the Moon for VIPER. MGRU3 would climb a $\theta = 10°$ slope at 18% slip, while the VIPER on the Moon would experience approximately 75% slip. Note that the data in Figure 22 is obtained by running a suite of experiments like the ones reported in Figure 11.

The main insights drawn from this study are as follows. The *nominal* rover that will undertake an extraterrestrial mission can be used on Earth for tests whose results can be extrapolated, via GSLs, to predict steady-state macro-behavior of the rover in extraterrestrial worlds. Second, for certain rovers (VIPER is such an example), testing efficiencies can be improved by using single-wheel tests instead of full-rover tests. Third, CRM simulation can produce detailed rover–terrain interaction information that cannot be easily obtained through physical testing. Even if one does not have a good idea about the parameters defining terrain models for other celestial bodies, being physics-based, CRM, and for that matter DEM, simulation can be used to perform parameter sweeps to reveal average behavior and worst case scenarios. Finally, one unexpected result was that the slope versus slip curves obtained in slope-mode test are invariant over a range of wheel angular velocities, see Figure 13.

Considering the body of evidence obtained in parabolic flights and via the revamped scaling laws, we believe that a paradigm shift is justified in extraterrestrial terramechanics in low-gravity fields. This contribution adds to this body of evidence, and it does so by employing a physics-based simulator that strays away from the BWJH model. The latter is empirical and cannot capture important factors that shape the performance of the rover, for example, nontrivial grouser geometries, impact of the gravity, nonflat terrain, dynamic effects (soil ejection, wheel sinking process). We posit that the wide adoption of the BWJH model, which is semiempirical, has prevented the community from understanding the fallacy of using gravitational offset since BWJH, in its common use, does not factor the gravitational acceleration in the terrain model. Considering the immediate future of lunar exploration provides even more impetus to move away from the BWJH models. Indeed, NASA's lunar habitation plans are anchored by in situ resource utilization that will require terramechanics studies of vehicles that dig into terrain, bulldoze it, and so forth. These operations call for physics that the BWJH class of models cannot capture.

Ultimately, the results obtained in this effort make a case for relying heavily on physics-based terramechanics models when designing rovers and landers for extraterrestrial exploration. Terramechanics simulation is presently coming of age for two reasons. First, leveraging GPU computing, as pursued here, results in substantial gains in simulation speed. This choice opens the door for the use of CRM and DEM, two modeling approaches previously dismissed as too slow to be relevant for large-scale terramechanics studies. The strength of both CRM and DEM is that they are physics-based. Therefore, (*ii*) by comparison with the BWJH class of models, the parameters used to set up the CRM or DEM digital-twin terrain are intuitive and more easily accessible; and (*iii*) the spectrum of applications in which CRM and DEM can come into play is richer than that of semiempirical methods of BWJH class, which was set up to address mobility only, and thus lacks the context necessary to handle other physics, for example, digging, bulldozing, or change in gravity. Second, and more importantly, using physics-based simulation provides insights that are otherwise difficult or impossible to obtain. How would these insights be otherwise obtained? As pointed out, using helium balloons or gantry-type systems for gravitational offset leads to overly optimistic results regarding trafficability outcomes. Then, the options left are parabolic flights and scaling laws. The former are challenging to set up for two reasons: the duration of an experiment is necessarily short; and collecting relevant information is challenging (it is difficult in a short parabolic flight to gauge how the material shears under a rover wheel since imaging these phenomena, while not impossible, is costly and cumbersome). Inexpensive solutions that employ transparent walls sometimes impact the very dynamics of the phenomena that are of interest and are by necessity providing only a 2D snapshot of the relevant physics. As for the GSLs, while elegant and insightful, they are limited to macro-scale information tied to *steady-state* regimes. Moreover, the insights provided pertain to the macro-scale performance of the vehicle and not that of the terrain. How the terrain is disturbed and how its dynamics is coupled with that of the implement is averaged out of the conversation. In other words, when using GSLs, one cannot tell much about how the terrain will be disturbed, which is an issue, for example, for the rear wheels moving over the ruts of the forward wheel, or when the ego rover or a companion one revisits the perturbed terrain.

Acknowledgments

Support for part of this study was provided by NASA STTR #80NSSC20C0252, National Science Foundation grant OAC2209791 and US Army Research Office, under grants W911NF1910431 and W911NF1810476. The first author was also supported by National Natural Science Foundation of China under grant 12302050. The authors are grateful to Dr. Colin Creager of NASA Glenn for his insightful comments on this manuscript and for sharing experimental results related to the MGRU physical testing.

Data Availability Statement

The data that support the findings of this study are available in crm_sim_nasa_exp_scripts at https://github.com/sjtumsd/crm_sim_nasa_exp_scripts. These data were derived from the following resources available in the public domain: crm_sim_nasa_exp_scripts, https://github.com/sjtumsd/crm_sim_nasa_exp_scripts.

References

Agarwal, S., A. Karsai, D. I. Goldman, and K. Kamrin. 2021. "Surprising Simplicity in the Modeling of Dynamic Granular Intrusion." *Science Advances* 7: eabe0631. https://doi.org/10.1126/sciadv.abe0631.

Agarwal, S., C. Senatore, T. Zhang, et al. 2019. "Modeling of the Interaction of Rigid Wheels With Dry Granular Media." *Journal of Terramechanics* 85: 1–14.

Apfelbeck, M., S. Kuß, B. Rebele, and B. Schäfer. 2011. "A Systematic Approach to Reliably Characterize Soils Based on Bevameter Testing." *Journal of Terramechanics* 48: 360–371.

Bardenhagen, S., J. Brackbill, and D. Sulsky. 2000. "The Material Point Method for Granular Materials." *Computer Methods in Applied Mechanics and Engineering* 187: 529–541.

Bauer, R., W. Leung, and T. Barfoot. 2005. "Experimental and Simulation Results of Wheel–Soil Interaction for Planetary Rovers." In *2005 IEEE/RSJ International Conference on Intelligent Robots and Systems*, 586–591. IEEE.

Baumgarten, A. S., and K. Kamrin. 2019. "A General Fluid–Sediment Mixture Model and Constitutive Theory Validated in Many Flow Regimes." *Journal of Fluid Mechanics* 861: 721–764.

Bekker, M. G. 1956. *Theory of Land Locomotion; the Mechanics of Vehicle Mobility*. University of Michigan Press.

Bekker, M. G. 1969. *Introduction to Terrain-Vehicle Systems*. University of Michigan Press.

Bian, X., and M. Ellero. 2014. "A Splitting Integration Scheme for the SPH Simulation of Concentrated Particle Suspensions." *Computer Physics Communications* 185: 53–62.

Binder, C., J. Hostetter, M. Kowalczyk, et al. 2022. Gravity Offload Rig for Lunar Rover Testing Wins Spring 2022 Capstone Design Showcase. Accessed March 9, 2024. https://www.minesnewsroom.com/news/gravity-offload-rig-lunar-rover-testing-wins-spring-2022-Capstone-design-showcase.

Bui, H. H., R. Fukagawa, K. Sako, and S. Ohno. 2008. "Lagrangian Meshfree Particles Method (SPH) for Large Deformation and Failure Flows of Geomaterial Using Elastic–Plastic Soil Constitutive Model." *International Journal for Numerical and Analytical Methods in Geomechanics* 32: 1537–1570.

Carsten, J., A. Rankin, D. Ferguson, and A. Stentz. 2009. "Global Planning on the Mars Exploration Rovers: Software Integration and Surface Testing." *Journal of Field Robotics* 26: 337–357.

Chauchat, J., and M. Médale. 2014. "A Three-Dimensional Numerical Model for Dense Granular Flows Based on the μ (I) Rheology." *Journal of Computational Physics* 256: 696–712.

Chen, J.-Y., F.-S. Lien, C. Peng, and E. Yee. 2020. "GPU-Accelerated Smoothed Particle Hydrodynamics Modeling of Granular Flow." *Powder Technology* 359: 94–106.

Chen, W., and T. Qiu. 2012. "Numerical Simulations for Large Deformation of Granular Materials Using Smoothed Particle Hydrodynamics Method." *International Journal of Geomechanics* 12: 127–135.

Chiang, H.-H., S.-J. Wu, J.-W. Perng, B.-F. Wu, and T.-T. Lee. 2010. "The Human-in-the-Loop Design Approach to the Longitudinal Automation System for an Intelligent Vehicle." *IEEE Transactions on Systems, Man, and Cybernetics—Part A: Systems and Humans* 40: 708–720.

Cundall, P. A., and O. D. Strack. 1979. "A Discrete Numerical Model for Granular Assemblies." *Geotechnique* 29: 47–65.

Daca, A. 2022. "Predicting Planetary Rover Mobility in Reduced Gravity Using 1-g Experiments." Ph.D. thesis, Concordia University. Unpublished. https://spectrum.library.concordia.ca/id/eprint/991773/.

Daca, A., D. Tremblay, and K. Skonieczny. 2022. "Experimental Evaluation of Cone Index Gradient as a Metric for the Prediction of Wheel Performance in Reduced Gravity." *Journal of Terramechanics* 99: 1–16.

DeDonato, M., V. Dimitrov, R. Du, et al. 2015. "Human-in-the-Loop Control of a Humanoid Robot for Disaster Response: A Report From the DARPA Robotics Challenge Trials." *Journal of Field Robotics* 32: 275–292.

Ding, L., Z. Deng, H. Gao, J. Tao, K. D. Iagnemma, and G. Liu. 2015. "Interaction Mechanics Model for Rigid Driving Wheels of Planetary Rovers Moving on Sandy Terrain With Consideration of Multiple Physical Effects." *Journal of Field Robotics* 32: 827–859.

Ding, L., R. Zhou, T. Yu, et al. 2022a. "Surface Characteristics of the Zhurong Mars Rover Traverse at Utopia Planitia." *Nature Geoscience* 15: 171–176.

Ding, L., R. Zhou, T. Yu, et al. 2024. "Lunar Rock Investigation and Tri-Aspect Characterization of Lunar Farside Regolith by a Digital Twin." *Nature Communications* 15: 2098.

Ding, L., R. Zhou, Y. Yuan, et al. 2022b. "A 2-year Locomotive Exploration and Scientific Investigation of the Lunar Farside by the Yutu-2 Rover." *Science Robotics* 7: eabj6660. https://doi.org/10.1126/scirobotics.abj6660.

Dunatunga, S., and K. Kamrin. 2015. "Continuum Modelling and Simulation of Granular Flows Through Their Many Phases." *Journal of Fluid Mechanics* 779: 483–513.

Dunatunga, S., and K. Kamrin. 2017. "Continuum Modeling of Projectile Impact and Penetration in Dry Granular Media." *Journal of the Mechanics and Physics of Solids* 100: 45–60.

Dungan, L. K., P. S. Valle, D. R. Bankieris, A. P. Lieberman, L. Redden, and C. Shy. 2015. "Active Response Gravity Offload and Method." U.S. Patent. Patent Office: U.S. Patent and Trademark Office.

Edwards, M. B., M. M. Dewoolkar, D. R. Huston, and C. Creager. 2017. “Bevameter Testing on Simulant Fillite for Planetary Rover Mobility Applications.” *Journal of Terramechanics* 70: 13–26.

Estier, T., Y. Crausaz, B. Merminod, M. Lauria, R. Piguet, and R. Siegwart. 2000. “An Innovative Space Rover With Extended Climbing Abilities.” In *Proceedings of the 4th International Conference and Exposition on Robotics for Challenging Situations and Environments, Albuquerque, NM, USA*, 333–339, American Society of Civil Engineering.

Farley, K. A., K. H. Williford, K. M. Stack, et al. 2020. “Mars 2020 Mission Overview.” *Space Science Reviews* 216: 1–41.

Fatehi, R., and M. T. Manzari. 2011. “Error Estimation in Smoothed Particle Hydrodynamics and a New Scheme for Second Derivatives.” *Computers & Mathematics With Applications* 61: 482–498.

Freitag, D. R., A. Green, and M. Klaus-Jurgen. 1970a. “Performance Evaluation of Wheels for Lunar Vehicles.” US Army Waterways Experiment Station—Technical Report No. M-70-2.

Freitag, D. R., R. L. Schafer, and R. D. Wismer. 1970b. “Similitude Studies of Soil–Machine Systems.” *Journal of Terramechanics* 7: 25–58.

Gingold, R. A., and J. J. Monaghan. 1977. “Smoothed Particle Hydrodynamics—Theory and Application to Non-Spherical Stars.” *Monthly Notices of the Royal Astronomical Society* 181: 375–389.

Gray, J. P., J. J. Monaghan, and R. Swift. 2001. “SPH Elastic Dynamics.” *Computer Methods in Applied Mechanics and Engineering* 190: 6641–6662.

Haeri, A., and K. Skonieczny. 2022. “Three-Dimensionsal Granular Flow Continuum Modeling via Material Point Method With Hyperelastic Nonlocal Granular Fluidity.” *Computer Methods in Applied Mechanics and Engineering* 394: 114904.

Han, O., D. Kienholz, P. Janzen, and S. Kidney. 2010. “Gravity-Off-Loading System for Large-Displacement Ground Testing of Spacecraft Mechanisms.” In *Proceedings of the 40th Aerospace Mechanisms Symposium*, NASA.

He, C. 2010. “Geotechnical Characterization of Lunar Regolith Simulants.” Ph.D. thesis, Case Western Reserve University.

He, C., X. Zeng, and A. Wilkinson. 2013. “Geotechnical Properties of GRC-3 Lunar Simulant.” *Journal of Aerospace Engineering* 26: 528–534.

Hegedus, E. 1960. *A Simplified Method for the Determination of Bulldozing Resistance*. US Army Ordnance Tank-Automotive Command.

Heverly, M., J. Matthews, J. Lin, et al. 2013. “Traverse Performance Characterization for the Mars Science Laboratory Rover.” *Journal of Field Robotics* 30: 835–846.

Holmes, D. W., J. R. Williams, and P. Tilke. 2011. “Smooth Particle Hydrodynamics Simulations of Low Reynolds Number Flows Through Porous Media.” *International Journal for Numerical and Analytical Methods in Geomechanics* 35: 419–437.

Hu, W., G. Guo, X. Hu, D. Negrut, Z. Xu, and W. Pan. 2019. “A Consistent Spatially Adaptive Smoothed Particle Hydrodynamics Method for Fluid–Structure Interactions.” *Computer Methods in Applied Mechanics and Engineering* 347: 402–424.

Hu, W., P. Li, H. M. Unjhawala, R. Serban, and D. Negrut. 2024. “Calibration of an Expeditious Terramechanics Model Using a Higher-Fidelity Model, Bayesian Inference, and a Virtual Bevameter Test.” *Journal of Field Robotics* 41: 550–569.

Hu, W., W. Pan, M. Rakhsha, Q. Tian, H. Hu, and D. Negrut. 2017. “A Consistent Multi-Resolution Smoothed Particle Hydrodynamics Method.” *Computer Methods in Applied Mechanics and Engineering* 324: 278–299.

Hu, W., M. Rakhsha, L. Yang, K. Kamrin, and D. Negrut. 2021. “Modeling Granular Material Dynamics and Its Two-Way Coupling With Moving Solid Bodies Using a Continuum Representation and the SPH Method.” *Computer Methods in Applied Mechanics and Engineering* 385: 114022.

Hu, W., Z. Zhou, S. Chandler, et al. 2022. “Traction Control Design for Off-Road Mobility Using an SPH–DAE Co-Simulation Framework.” *Multibody System Dynamics* 55: 165–188.

Hurley, R. C., and J. E. Andrade. 2017. “Continuum Modeling of Rate-Dependent Granular Flows in SPH.” *Computational Particle Mechanics* 4: 119–130.

Iagnemma, K., S. Kang, H. Shibly, and S. Dubowsky. 2004. “Online Terrain Parameter Estimation for Wheeled Mobile Robots With Application to Planetary Rovers.” *IEEE Transactions on Robotics* 20: 921–927.

Iagnemma, K., H. Shibly, and S. Dubowsky. 2002. “On-Line Terrain Parameter Estimation for Planetary Rovers.” In *Proceedings of the 2002 IEEE International Conference on Robotics and Automation*, Vol. 3, 3142–3147. IEEE.

Ionescu, I. R., A. Mangeney, F. Bouchut, and O. Roche. 2015. “Viscoplastic Modeling of Granular Column Collapse With Pressure-Dependent Rheology.” *Journal of Non-Newtonian Fluid Mechanics* 219: 1–18.

Irani, R., R. Bauer, and A. Warkentin. 2011. “A Dynamic Terramechanic Model for Small Lightweight Vehicles With Rigid Wheels and Grousers Operating in Sandy Soil.” *Journal of Terramechanics* 48: 307–318.

Ishigami, G., A. Miwa, K. Nagatani, and K. Yoshida. 2007. “Terramechanics-Based Model for Steering Maneuver of Planetary Exploration Rovers on Loose Soil.” *Journal of Field Robotics* 24: 233–250.

Iwashita, K., and M. Oda. 1999. *Mechanics of Granular Materials: An Introduction*. CRC Press.

Janosi, Z., and B. Hanamoto. 1961. “The Analytical Determination of Drawbar Pull as a Function of Slip for Tracked Vehicles in Deformable Soils.” In *Proceedings of the 1st International Conference on Terrain-Vehicle Systems, Turin, Italy*.

Jensen, R. P., P. J. Bosscher, M. E. Plesha, and T. B. Edil. 1999. “DEM Simulation of Granular Media–Structure Interface: Effects of Surface Roughness and Particle Shape.” *International Journal for Numerical and Analytical Methods in Geomechanics* 23: 531–547.

Johnson, J. B., A. V. Kulchitsky, P. Duvoy, et al. 2015. “Discrete Element Method Simulations of Mars Exploration Rover Wheel Performance.” *Journal of Terramechanics* 62: 31–40.

Jop, P., Y. Forterre, and O. Pouliquen. 2005. “Crucial Role of Sidewalls in Granular Surface Flows: Consequences for the Rheology.” *Journal of Fluid Mechanics* 541: 167–192.

Kerr, R. A. 2009. *Mars Rover Trapped in Sand, But What Can End a Mission?*. American Association for the Advancement of Science.

Kobayashi, T., Y. Fujiwara, J. Yamakawa, N. Yasufuku, and K. Omine. 2010. “Mobility Performance of a Rigid Wheel in Low Gravity Environments.” *Journal of Terramechanics* 47: 261–274.

Kovács, L. L., B. Ghotbi, F. González, P. Niksirat, K. Skonieczny, and J. Kövecses. 2020. “Effect of Gravity in Wheel/Terrain Interaction Models.” *Journal of Field Robotics* 37: 754–767.

Krenn, R., and A. Gibbesch. 2011. “Soft Soil Contact Modeling Technique for Multi-Body System Simulation.” In *Trends in Computational Contact Mechanics*, 135–155. Springer.

Krenn, R., A. Gibbesch, and G. Hirzinger. 2008. “Contact Dynamics Simulation of Rover Locomotion.” In *9th International Symposium on Artificial Intelligence, Robotics and Automation in Space (iSAIRAS), Universal City, CA*.

Krenn, R., and G. Hirzinger. 2009. “SCM—A Soil Contact Model for Multi-Body System Simulations.” In *11th European Regional Conference of the International Society for Terrain-Vehicle Systems—ISTVS 2009*. http://elib.dlr.de/60535/.

Lucy, L. B. 1977. "A Numerical Approach to the Testing of the Fission Hypothesis." *Astronomical Journal* 82: 1013–1024.

Meirion-Griffith, G., and M. Spenko. 2011. "A Modified Pressure-Sinkage Model for Small, Rigid Wheels on Deformable Terrains." *Journal of Terramechanics* 48: 149–155.

Monaghan, J. J. 1989. "On the Problem of Penetration in Particle Methods." *Journal of Computational Physics* 82: 1–15.

Monaghan, J. J. 1994. "Simulating Free Surface Flows With SPH." *Journal of Computational Physics* 110: 399.

Monaghan, J. J. 2000. "SPH Without a Tensile Instability." *Journal of Computational Physics* 159: 290–311.

Monaghan, J. J. 2005. "Smoothed Particle Hydrodynamics." *Reports on Progress in Physics* 68: 1703–1759.

Morris, J. P., P. J. Fox, and Y. Zhu. 1997. "Modeling Low Reynolds Number Incompressible Flows Using SPH." *Journal of Computational Physics* 136: 214–226.

Morris, R. V., G. Klingelhofer, B. Bernhardt, et al. 2004. "Mineralogy at Gusev Crater From the Mossbauer Spectrometer on the Spirit Rover." *Science* 305: 833–836.

Negrut, D., R. Serban, and A. Tasora. 2018. "Posing Multibody Dynamics With Friction and Contact as a Differential Complementarity Problem." *Journal of Computational and Nonlinear Dynamics* 13: 014503.

Nguyen, C. T., C. T. Nguyen, H. H. Bui, G. D. Nguyen, and R. Fukagawa. 2017. "A New SPH-Based Approach to Simulation of Granular Flows Using Viscous Damping and Stress Regularisation." *Landslides* 14: 69–81.

Ojeda, L., J. Borenstein, G. Witus, and R. Karlsen. 2006. "Terrain Characterization and Classification With a Mobile Robot." *Journal of Field Robotics* 23: 103–122.

Oravec, H. A., X. Zeng, and V. Asnani. 2010. "Design and Characterization of GRC-1: A Soil for Lunar Terramechanics Testing in Earth-Ambient Conditions." *Journal of Terramechanics* 47: 361–377.

Oravec, H. A., V. M. Asnani, C. M. Creage, and S. J. Moreland. 2021. "Geotechnical Review of Existing Mars Soil Simulants for Surface Mobility." In *Earth and Space 2021*, 157–170.

Pan, W., K. Kim, M. Perego, A. M. Tartakovsky, and M. L. Parks. 2017. "Modeling Electrokinetic Flows by Consistent Implicit Incompressible Smoothed Particle Hydrodynamics." *Journal of Computational Physics* 334: 125–144.

Pazouki, A., M. Kwarta, K. Williams, et al. 2017. "Compliant Versus Rigid Contact: A Comparison in the Context of Granular Dynamics." *Physical Review E* 96: 042905. https://doi.org/10.1103/PhysRevE.96.042905.

Pearson, E. 2024. *How Scientists Are Tackling the Biggest Problems of Returning Humans to the Moon*. BBC Science Focus. https://www.sciencefocus.com/space/moon-on-earth.

Project Chrono Team. 2020. *Chrono: An Open Source Framework for the Physics-Based Simulation of Dynamic Systems*. Accessed January 10, 2022. https://github.com/projectchrono/chrono.

Recuero, A. M., R. Serban, B. Peterson, H. Sugiyama, P. Jayakumar, and D. Negrut. 2017. "A High-Fidelity Approach for Vehicle Mobility Simulation: Nonlinear Finite Element Tires Operating on Granular Material." *Journal of Terramechanics* 72: 39–54.

Rodríguez-Martínez, D., M. Van Winnendael, and K. Yoshida. 2019. "High-Speed Mobility on Planetary Surfaces: A Technical Review." *Journal of Field Robotics* 36: 1436–1455.

Senatore, C., N. Stein, F. Zhou, et al. 2014. "Modeling and Validation of Mobility Characteristics of the Mars Science Laboratory Curiosity Rover." In *Proceedings of the 12th International Symposium on Artificial Intelligence, Robotics and Automation in Space (i-SAIRAS)*.

Serban, R., J. Taves, and Z. Zhou. 2022. "Real Time Simulation of Ground Vehicles on Deformable Terrain." In *Proceedings of the ASME IDETC/CIE 2022, St. Louis, MO*, American Society of Mechanical Engineers.

Shibly, H., K. Iagnemma, and S. Dubowsky. 2005. "An Equivalent Soil Mechanics Formulation for Rigid Wheels in Deformable Terrain, With Application to Planetary Exploration Rovers." *Journal of Terramechanics* 42: 1–13.

Skonieczny, K., D. Wettergreen, and W.-R. Whittaker. 2016. "Advantages of Continuous Excavation in Lightweight Planetary Robotic Operations." *International Journal of Robotics Research* 35: 1121–1139.

Slonaker, J., D. C. Motley, Q. Zhang, et al. 2017. "General Scaling Relations for Locomotion in Granular Media." *Physical Review E* 95: 052901.

Smith, W., D. Melanz, C. Senatore, K. Iagnemma, and H. Peng. 2014. "Comparison of Discrete Element Method and Traditional Modeling Methods for Steady-State Wheel–Terrain Interaction of Small Vehicles." *Journal of Terramechanics* 56: 61–75.

Soga, K., E. Alonso, A. Yerro, K. Kumar, and S. Bandara. 2016. "Trends in Large-Deformation Analysis of Landslide Mass Movements With Particular Emphasis on the Material Point Method." *Géotechnique* 66: 248–273.

Sulsky, D., Z. Chen, and H. L. Schreyer. 1994. "A Particle Method for History-Dependent Materials." *Computer Methods in Applied Mechanics and Engineering* 118: 179–196.

Takeda, H., S. M. Miyama, and M. Sekiya. 1994. "Numerical Simulation of Viscous Flow by Smoothed Particle Hydrodynamics." *Progress of Theoretical Physics* 92: 939–960.

Tang, Z., J. Liu, X. Wang, et al. 2020. "Physical and Mechanical Characteristics of Lunar Soil at the Chang'E-4 Landing Site." *Geophysical Research Letters* 47: e2020GL089499. https://doi.org/10.1029/2020GL089499.

Tasora, A., R. Serban, H. Mazhar, et al. 2016. "Chrono: An Open Source Multi-Physics Dynamics Engine." In *High Performance Computing in Science and Engineering—Lecture Notes in Computer Science*, edited by T. Kozubek, 19–49. Springer International Publishing.

Taylor, L. A., C. M. Pieters, and D. Britt. 2016. "Evaluations of Lunar Regolith Simulants." *Planetary and Space Science* 126: 1–7.

Thoesen, A., T. McBryan, D. Mick, M. Green, J. Martia, and H. Marvi. 2020a. "Comparative Performance of Granular Scaling Laws for Lightweight Grouser Wheels in Sand and Lunar Simulant." *Powder Technology* 373: 336–346.

Thoesen, A., T. McBryan, D. Mick, M. Green, J. Martia, and H. Marvi. 2020b. "Granular Scaling Laws for Helically Driven Dynamics." *Physical Review E* 102: 032902.

Ucgul, M., J. Fielke, and C. Saunders. 2015. "Three-Dimensional Discrete Element Modeling (DEM) of Tillage: Accounting for Soil Cohesion and Adhesion." *Biosystems Engineering* 129: 298–306.

Valle, P. 2017. "Reduced Gravity Testing of Robots (and Humans) Using the Active Response Gravity Offload System." In *International Conference on Intelligent Robots and Systems (IROS), JSC-CN-40487*.

Voosen, P. 2018. *NASA Curiosity Rover Hits Organic Pay Dirt on Mars*, American Association for the Advancement of Science.

Wall, M. 2024. *Japan's SLIM Moon Lander Photographed on the Lunar Surface—On Its Nose (Image)*. Accessed February 10, 2025. https://www.space.com/japan-slim-moon-lander-photo-lunar-surface.

Wismer, R., D. Freitag, and R. Schafer. 1976. "Application of to Soil–Machine Systems." *Journal of Terramechanics* 13: 153–182.

Wong, J. 2012. "Predicting the Performances of Rigid Rover Wheels on Extraterrestrial Surfaces Based on Test Results Obtained on Earth." *Journal of Terramechanics* 49: 49–61.

Wong, J. Y. 2009. *Terramechanics and Off-Road Vehicle Engineering: Terrain Behaviour, Off-Road Vehicle Performance and Design*. Butterworth-Heinemann.

Wong, J. Y., and A. R. Reece. 1967a. "Prediction of Rigid Wheel Performance Based on the Analysis of Soil–Wheel Stresses: Part II. Performance of Towed Rigid Wheels." *Journal of Terramechanics* 4: 7–25.

Wong, J. Y., and A. R. Reece. 1967b. "Prediction of Rigid Wheel Performance Based on the Analysis of Soil–Wheel Stresses Part I. Performance of Driven Rigid Wheels." *Journal of Terramechanics* 4: 81–98.

Xu, W.-J., X.-Y. Dong, and W.-T. Ding. 2019. "Analysis of Fluid–Particle Interaction in Granular Materials Using Coupled SPH–DEM Method." *Powder Technology* 353: 459–472.

Yue, Y., B. Smith, C. Batty, C. Zheng, and E. Grinspun. 2015. "Continuum Foam: A Material Point Method for Shear-Dependent Flows." *ACM Transactions on Graphics (TOG)* 34: 1–20.

Zhan, L., C. Peng, B. Zhang, and W. Wu. 2019. "Three-Dimensional Modeling of Granular Flow Impact on Rigid and Deformable Structures." *Computers and Geotechnics* 112: 257–271.

Zhang, Q., S. Townsend, and K. Kamrin. 2020. "Expanded Scaling Relations for Locomotion in Sloped or Cohesive Granular Beds." *Physical Review Fluids* 5: 114301.

Zhao, C.-L., and M.-Y. Zang. 2017. "Application of the FEM/DEM and Alternately Moving Road Method to the Simulation of Tire–Sand Interactions." *Journal of Terramechanics* 72: 27–38.

Supporting Information

Additional supporting information can be found online in the Supporting Information section.